12-1988

An Analysis of Topographic Effects on LANDSAT Thematic Mapper Image Using Digital Terain Data

Xiaomin Liu

University of Tennessee - Knoxville

Recommended Citation

Liu, Xiaomin, "An Analysis of Topographic Effects on LANDSAT Thematic Mapper Image Using Digital Terain Data. " Master's Thesis, University of Tennessee, 1988.
https://trace.tennessee.edu/utk_gradthes/3280

To the Graduate Council:

I am submitting herewith a thesis written by Xiaomin Liu entitled "An Analysis of Topographic Effects on LANDSAT Thematic Mapper Image Using Digital Terain Data." I have examined the final electronic copy of this thesis for form and content and recommend that it be accepted in partial fulfillment of the requirements for the degree of Master of Science, with a major in Forestry.

John C. Rennie, Major Professor

We have read this thesis and recommend its acceptance:

James R. Carter, John B. Rehder

Accepted for the Council:
Carolyn R. Hodges

Vice Provost and Dean of the Graduate School

(Original signatures are on file with official student records.)

To the Graduate Council:

I am submitting herewith a thesis written by Xiaomin Liu entitled "An Analysis of Topographic Effects on LANDSAT Thematic Mapper Using Digital Terain Data." I have examined the final copy of this thesis for form and content and recommend that it be accepted in partial fulfillment of the requirements for the degree of Master of Science, with a major in Forestry.

JC Rennie

John C. Rennie, Major Professor

We have read this thesis
and recommend its acceptance:

James R. Carter

John B. Rehder

Accepted for the Council:

CWMinkel

Vice Provost
and Dean of The Graduate School

AN ANALYSIS OF TOPOGRAPHIC EFFECTS ON LANDSAT THEMATIC MAPPER IMAGE USING DIGITAL TERRAIN DATA

A Thesis
Presented for the
Master of Science
Degree
The University of Tennessee, Knoxville

Xiaomin Liu
December 1988

Acknowledgements

I would like to express my gratitude to several people who assisted me generously in the course of thesis research. Great appreciation is given to my major professor, Dr. John C. Rennie, for his suggestion of this research topic and guidance throughout the course of the study. Particular thanks are due Dr. Rennie, for his consistent patience, encouragement, and confidence during my study in the University of Tennessee.

I also want to extend my special thanks to Dr. James R. Carter, an Associate Director of the University of Tennessee Computing Center and Associate Professor of Geography, for his advice, consultation, criticism, and supply of digital elevation model as well as some programs; to Dr. John B. Rehder, Department of of Geography, for his many valuable suggestions and for serving as committee member.

Special thanks are given to Mr. Mark MacKenzie who offered me great assistance and provided LANDSAT test data.

This study was supported by the Department of Forestry, Wildlife, and Fisheries, the University of Tennessee, Knoxville. The use of the University of Tennessee Computing Center is acknowledged.

Finally, I cannot thank enough my wife, Ling, for her understanding and support.

Abstract

A comprehensive literature review on the simulation and corrections of topographic variations in remote sensing data was presented. The effects of topography on the scene radiance of LANDSAT thematic mapper (TM) image were examined in the context of the remote sensing of vegetation in Great Smoky Mountains National Park (GSMNP).

To simulate the image intensity component due to varying orientation of surface elements, two reflectance models were adopted to generate the synthetic images from a Digital Elevation Model (DEM). Visual and analytical procedures were developed to register the TM image to the DEM data.

The dark tones of scene radiance of most TM bands effective to vegetation classification were found to be caused by the terrain relief surface with incidence angle more than 55^o rather than the intrinsic scene properties.

Statistically significant correlation were found between LANDSAT TM data and the synthetic brightness values. The best correlation coefficient was 0.854. This result indicated that a simple linear model gives a good prediction of measured brightness as a function of the cosine of the incident angle of the direct solar beam.

The residual images were produced from the linear regression model of real LANDSAT TM and synthetic images. The segmentation of residual images was performed based on the two segmenting criteria to extract ground spectral patterns. The outcome is discussed with a view to achieving a better understanding of the nature of problem.

Contents

List of Figures

List of Tables

Chapter 1

Introduction

1.1 Background

In remote sensing of Earth resources, optical-electronic sensors on a satellite or airplane receive the spectral brightness reflected from or emitted by the ground and objects on it in different wavelength bands. These data are recorded on computer compatible tapes or sent to ground receiving stations for processing. The spectral reflectance value apparently is the combination of the effects of variations in viewing direction, incident illumination, surface slope and surface material.

A major application of remote sensing in forestry is classifying and mapping of ground cover types, based on different cover types having different reflectance properties. In mountainous areas, the changes in scene radiance are due not only to variation in ground cover but also variation in topography. In many cases the topographic effects are dominant. Thus classifying and mapping of ground cover types should be based on measurable properties of the surface, not just raw image intensities, because the latter are only indirectly related to the surface properties. That is, the effects of surface material and topography must be separated from each other under specific illumination conditions. However, separating changes in scene radiance due to topography from changes due to ground cover is difficult because their effects are confounded and cannot be distinguished in a single view (Woodham and Lee, 1985), that is, using only one set of images without a stereo models.

The shaded-relief image (also called the synthetic image) produced from topographic terrain data with a reflectance model is a possible way to incorporate solar illumination, surface orientation, and viewing direction into a single model. Such a model allows image irradiance to be related directly to surface orientation. If a shaded-relief image can correctly predicate the variations of irradiance caused by topography, the remaining component of irradiance is directly related to surface features. This study attempts to utilize two reflectance models and topographic terrain data to simulate topographic variation; the topographic effect existing in raw remotely sensed data can then be reduced and vegetation types predicted with greater accuracy.

Classifying and mapping of vegetation types in Great Smoky Mountains National Park (GSMNP) has been carried out for two years as a cooperative project between the University of Tennessee Geography Department and the National Park Service. So far, the park-wide mapping of spruce, fir, hemlock, and pine forests has been completed using digital LANDSAT MSS data (Rehder, 1987). More than 10 classes of major deciduous vegetation types have been classified and mapped in two quadrangle test areas within the Park

(MacKenzie, 1988a). Also, studies on topography of this complex area have been conducted and slope maps by categories have been produced for the entire Park (Carter, 1987).

1.2 Objectives

The objectives of this study are:

** To simulate and quantify terrain orientation and solar position with reflectance models using digital elevation model (DEM) data.

** To register LANDSAT thematic mapper (TM) image with DEM data in Universal Transverse Mecator (UTM) coordinate frame.

** To evaluate the relationships among LANDSAT TM images and synthetic brightness values from both reflectance models.

Chapter 2

Literature Review

2.1 General Remarks

Digital classification of LANDSAT data has produced mixed results in natural resource inventories. Incorrect results arise from various random and systematic variation in physical phenomena which give rise to radiometric distortions in a scene. The accurate and quantitative interpretation of remotely sensed data requires that digital images be corrected radiometrically and geometrically prior to analysis. Extensive investigations have been conducted at the Canada Center for Remote Sensing (CCRS) on image correction in remote sensing (Teillet et al., 1982; Goodenough, 1979; Woodham and Lee, 1985; and Woodham et al. 1987). They grouped radiometric effects on the spectral signatures of objects into four major categories: (i) illumination conditions, (ii) observation geometry, (iii) atmospheric phenomena, and (iv) topographic variations. Among these factors, topographic effect is the most dominant and most difficult to correct in mountainous areas since it is involved with the effects of illumination conditions, atmospheric scattering, and viewing position. Topographic effect is defined as the variation in radiance from an inclined surface compared to radiance from a horizontal surface as a function of the surface orientation relative to the light source and sensor position (Holben and Justice, 1981). This effect complicates multispectral cover classification using remotely sensed satellite data in mountainous terrain. Therefore, developing procedures to obtain useful information regarding surface cover is an important area of concern in remote sensing.

Radiometric corrections for topographic effect have been investigated since the beginning of remote sensing. Most efforts have focused on improving the accuracy of remote sensing measurements of surface reflection properties such as albedo in rough terrain (Fleming and Hoffer, 1979; and Kusaka et al., 1984). Various correction procedures have been tested to improve classification accuracy in mountainous regions. Generally, these methods can be divided into two categories: those methods that manipulate raw spectral data without external information and those that utilize ancillary data. Examples of the first approach are the channel ratio techniques. The spectral band ratioing approach was proposed to enhance the digital image of LANDSAT and reduce the shadow influence. However, Justice et al. (1981) and Hall-Knoyves (1984) demonstrated that the effectiveness of ratioing for removing the topographic effect is a complex matter and that successful classification will be dependent on a number of interrelated factors, such as sun angle, spatial distribution of slopes and orientations, skylight and atmospheric conditions, surface reflectance properties.

To quantify the topographic relief effect found in LANDSAT data, ancillary data, such as digitized maps and terrain (elevation, slope, and aspect) data, have been combined with LANDSAT data in various means. Generally, these data have been used in three ways (Hutchinson, 1982):

a. Preclassification scene stratification:

Stratification divides a large study area into smaller strata based on some criterion or rule, so that each stratum can be represented by a homogeneous unit or objects with ecological similarity; each stratum is processed separately. This approach results in smaller data sets at each stage of analysis. The more important advantage is a reduction in the variation of objects of interest within each study area. However, stratification cannot accommodate graduation or fuzzy boundaries between strata due to its deterministic nature (Hutchinson, 1982).

b. Modifications in classifier operation:

Ancillary data can be incorporated during the classification in three approaches: (1) The "logical channel" treats elevation, slope angle, and slope aspect as additional channels in a multispectral classification system (Strahler, 1981). (2) The "unequal prior probability" uses terrain variables to modify prior probabilities of classification in a maximum likelihood decision rule according to the known association between object classes and the ancillary data (Strahler, 1980). (3) The "layered" technique develops the topographic distribution model to determine the probability of each forest type occurring at any given elevation, slope, and aspect; it then uses these topographic statistics to further subdivide forest types to the species level after classifying major cover types with spectral statistics (Fleming and Hoffer, 1979).

c. Postclassification class sorting:

Postclassification sorting is a variation on the technique of overlay analysis in geographic information systems. This method is effectively used for treating the problem where a single class of objects is represent by more than one spectral class. Although it, like stratification, is deterministic, it does offer some advantages: it is quick, easily implemented, and relatively simple to include several types of ancillary data in developing decision rules (Hutchinson, 1982).

2.2 Reflectance Model

Correction of a remote sensing image must address reflectance properties. Any correction method usually employs some a priori knowledge of the reflection properties of the surface of interest, i.e., a reflection model. The correction accuracy is basically limited by the discrepancy between model and reality.

Before examining the relationship between the radiance models and the remotely sensed spectral data, the nature of these models must be explored. The principal angles in the formation of the models are the incidence and viewing angles (see Figure 1). The incidence angle (i) is the angle formed between the sun and the surface normal. The viewing angle (e) is formed between the sensor and the surface normal. As shown in Figure 2, the radiance received by a sensor can theoretically be viewed as a function of the amount of light falling on the surface, the scattering properties of the surface, and the scattering properties of the transmitting medium between the sensor and the Earth's surface. The light falling on the ground surface can be divided in terms of direct and diffuse radiance. The direct irradiance is the parallel light radiating directly from the sun. The diffuse light is multidirectional and is composed of light scattered onto the surface by the atmosphere or surrounding ground surface. Under a clear sky (i.e., non-hazy conditions), the diffuse component is a small proportion of the total irradiance, e.g., less than 12% of the total in a study by Smith et al. (1980). The scattering properties of the surface are a function of the surface composition and roughness; thus they are difficult to model.

Two special cases of scattering, however, are relatively easy to model for direct radiance. A complete specular surface is one from which the radiance is monodirectional in the angle of reflectance, just like a mirror. The second special case is the Lambertian surface which scatters light equally in all directions and therefore can be modelled simply as a function of the cosine of the incidence angle (Monteith, 1962 as cited in Horn, 1981) as shown in Equation (2.1).

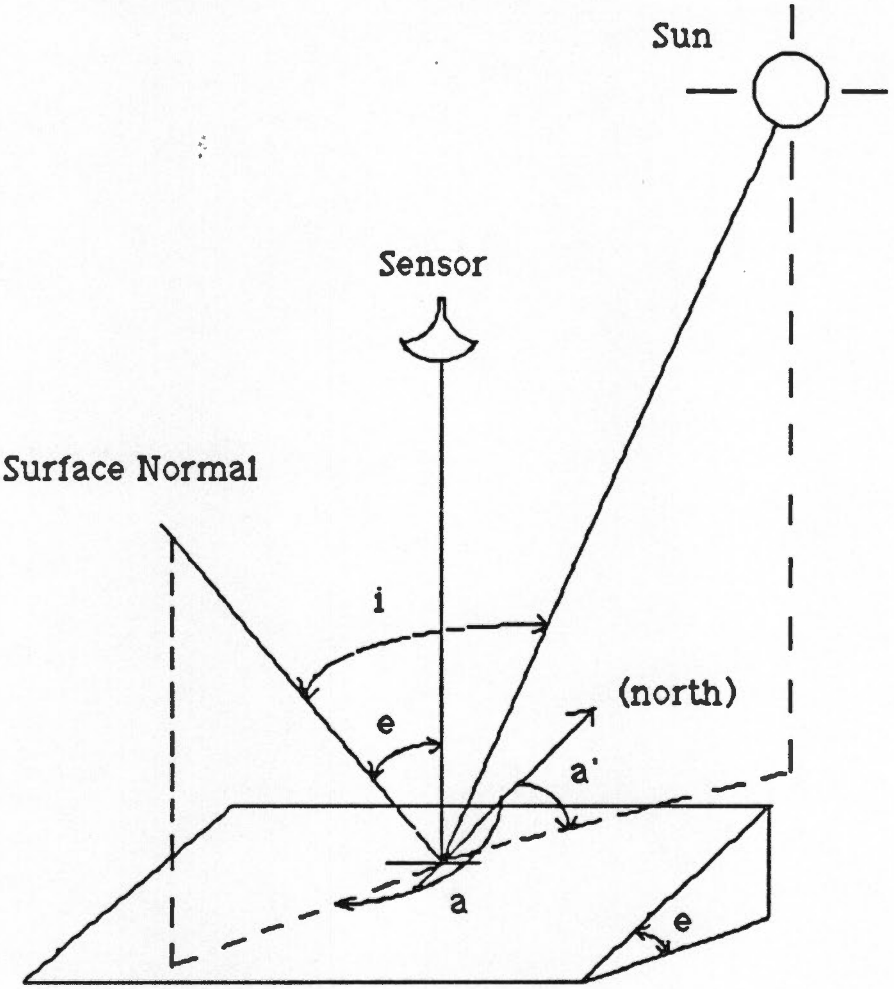

i = incidence angle
e = viewing angle = slope
a = azimuth of slope normal
a' = solar azimuth
|a - a'| = azpect angle

Figure 1. Principal angles used in radiance models

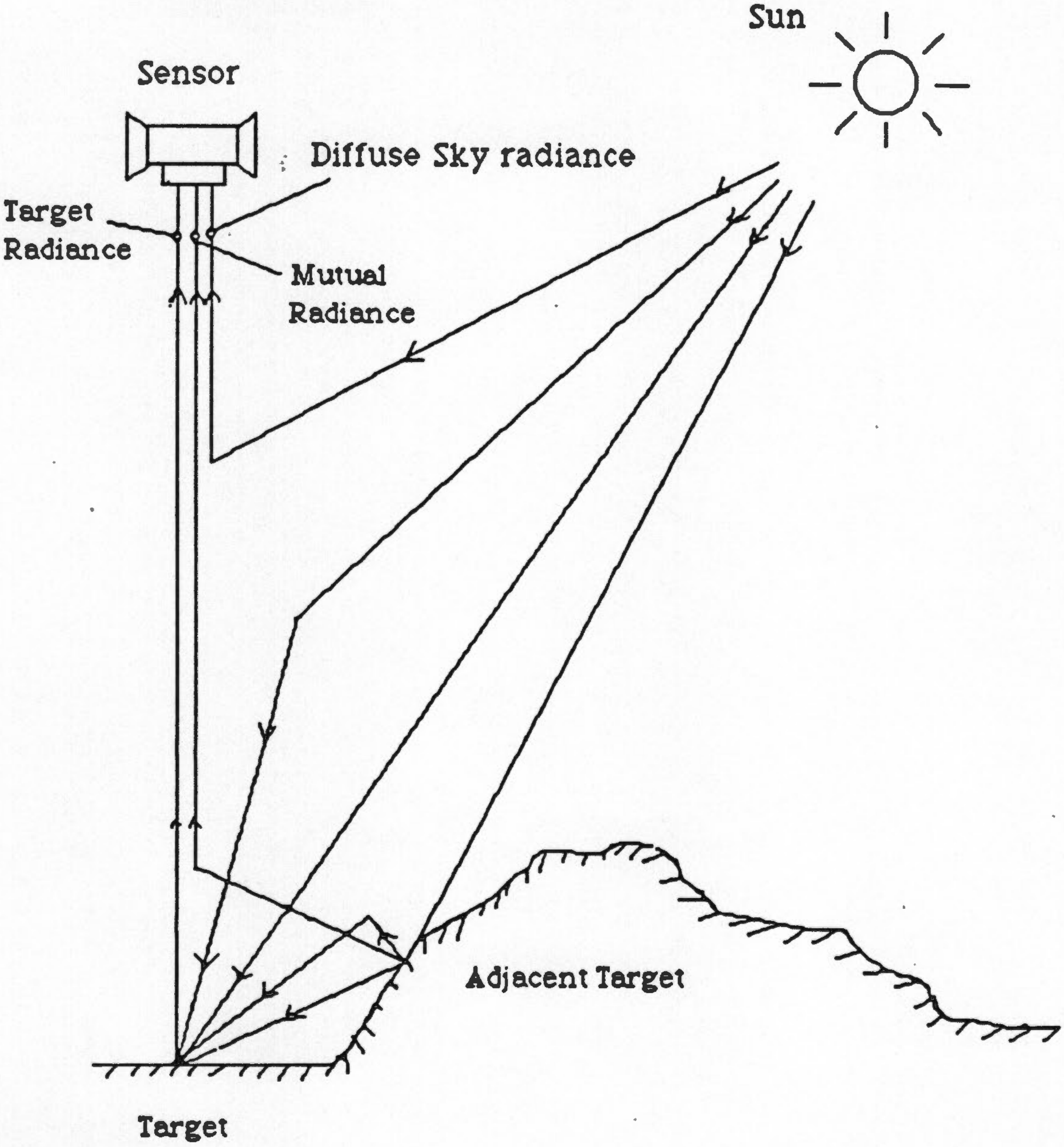

Figure 2. Components of scene radiance in remote sensing (Wood-ham and Gray, 1987). (Target receives direct solar radiance and diffuse sky radiation. Diffuse sky radiation has components due to scattered solar radiation and radiation from adiacent targets. Scene radiance also includes path radiance and radiation reflected from adjacent targets.)

$$R = Rn * \cos(i) \tag{1}$$

where: R = radiance

Rn = radiance (when $i = 0$)

i = incidence angle

The suitability of a theoretical Lambertian model to simulate the topographic effect was tested by Holben and Justice (1979). They collected hand-held radiometric data from a uniform sand surface oriented through a complete range of slope angles and aspects for several solar elevations. The radiance measurements from this experiment were correlated with values predicated by a simple Lambertian model. The analysis showed considerable variation in radiance values for different slope angles and aspects, and that these values varied considerably with changes in solar elevation and azimuth. This study revealed that the Lambertian assumption is only valid for certain cases and that LANDSAT data could be stratified according to surface incidence angle as well as surface cover type to provide improved cover classification.

Most natural surfaces are non-Lambertian; that is, they have preferred directions of scattering (Kriebel, 1978; Hugli, 1983). Radiance from a non-Lambertian surface, therefore, must be modelled by considering both incidence and the directional scattering from the surface. Smith et al. (1980) proposed a model which included incidence and viewing angles as a function of an empirical constant, "K"

$$R = Rn * [\cos^{K}(i) * \cos^{K-1}(e)] \qquad (2)$$

here: e = viewing angle

K = Minnaert constant

The empirical constant "K" was developed by Minnaert (Horn, 1981) and was used for photometric analysis of the lunar surface. The "K" value can be derived by linearizing equation (2):

$$\log[R * \cos(e)] = \log(Rn) + K * \log[\cos(i) * \cos(e)] \qquad (3)$$

Letting: $y = \log[R * \cos(e)]$, the response variable,

$x = \log[\cos(i) * \cos(e)]$, the independent variable

$b = \log(Rn)$

thus, the linear form can be obtained as equation (4)

$$y = K * x + b. \qquad (4)$$

Smith presented the some discription for the value, K:

> Generally, K varies with phase angle defined as the angle between the sensor and the illumination source. The Minnaert constant "K" describes the type of scattering dependence and is related to surface roughness. If K = 1, a Lambertian surface is defined and Equation (2) reduces to Equation (1). Low values of K imply a porous surface which exhibits asymmetrical diffuse scattering (Young and Collius, 1971). Values of K unequal to 1.0 imply a combination of diffuse and specular scattering.

The comparison test for the Lambertian model and the non-Lambertian model was conducted with hand-held radiometer and a uniform sand surface at four different solar elevations (Justice and Holben, 1979). Linear correlation coefficients for the non-Lambertian model and the field spectra were calculated to be greater than 0.92 for all cases, whereas correlation coefficients for the Lambertian model ranged from 0.06 to 0.98. These results demonstrated that the Lambertian model was less suitable than the non-Lambertian model for simulating the spectral response at high solar elevations.

Detailed examination of the empirical constant "K" revealed that it varied not only as a function of phase angle and wavelength for a cover type but varied considerably with surface geometry, i.e., slope and aspect (Smith et al., 1980; Justice and Hoblen, 1979).

Smith et al. (1980) used both the Lambertian and non-Lambertian models on a specific vegetative cover, ponderosa pine (*Pinus ponderosa*), to test their suitability with LANDSAT MSS data. They concluded that the Lambertian assumption is not strictly valid for LANDSAT data of ponderosa pine and indicated that the Lambertian approximation is more nearly valid when suitable restrictions are imposed on the range of incidence or viewing angles. As seen from the discussion above, the Lambertian assumption requires only slope and aspect data for any given LANDSAT pixel but it is only effective for certain cases. The non-Lambertian model is valid over a wide range of slopes and 'azpects', but requires radiance information for specific cover types to calculate the empirical "K" value. Here, 'azpect' is defined as the aspect of a surface slope relative to the sun's azimuth or so called relative azimuth (Holben and Justice, 1979; Teillet et al., 1982). However, calculating "K" for each cover type and each azpect is not practical.

Since the Lambertian model provides an average approximation of the reflection characteristic of the solid part of the Earth's surface, and also because of its simply mathematical form, as well as not requiring any ground cover type information, the Lambertian model is used routinely for radiometric correction in some visual interpretation and automatic classification of the ground cover type or terrain (Kusaka et al. 1984; Horn and Bachman, 1978; Seidel et al. 1983). There are other models more complex than the non-Lambertian model (e.g., Hugli et al., 1983; Blinn, 1977; Egbert, 1977; Favre et al., 1979; Horn, 1981), but these are beyond the discussion in this study.

2.3 Radiometric Correction for Topography

In many applications with raw remotely sensed data, the ground surface was considered to be flat and the brightness values recorded were then considered as the scene irradiance of targets. In mountainous terrain, the problem is more complex since the sloping terrain will give rise to different radiance values observed by the satellite sensor according to the angle of incidence and the amount of sky illumination. The radiometry, as a result, is the consequence of combined effect of reflection properties and surface orientation. The digital counts of LANDSAT TM data should therefore be modified to account for the spatially varying surface orientation and other contributing variations, such as viewer position and atmospheric conditions.

Teillet et al. (1982) tested the Lambertian and non-Lambertian illumination corrections taking into account atmospheric effects as well as topographic variations. Emphasis was placed on the special case of a simple cosine correction analogous to the sun angle corrections used widely for images of horizontal terrain. They formulated the slope-aspect correction function of a Lambertian reflector and the four other non-Lambertian correction functions; the software implementing these correction functions has been developed on the CCRS Image Analysis System (CIAS) at the Canada Centre for Remote Sensing (CCRS) (Goodenough, 1979).

The correction function based on Lambertian model is (Teillet, Guindon, and Goodenough, 1982):

$$L_H = \left(L_T - L_P\right)\left(\frac{\cos(Z) + f}{\cos(i) + hf}\right) + L_P \qquad (5)$$

where:

L_H = radiance observed for horizontal surface

L_T = radiance observed over sloping terrain

L_P = atmospheric path radiance

Z = solar zenith angle = incident angle for horizontal surface

i = incident angle with respect to surface normal

f = $H_D/(H_S T_D)$

H_S = solar irradiance at the top of the atmosphere

H_D = diffuse sky irradiance on a horizontal surface

T_D = $\exp(-t/\cos(Z))$

t = atmospheric extinction coefficient

h = $1 - s/\pi$

s = terrain slope

In this correction function, the multiple reflections due to surrounding slopes are not taken into account. If atmospheric information is ignored in Equation (5), then both path radiance and sky irradiance should be zero, that is $L_P = f = 0$, and one is left with a cosine correction:

$$L_H = L_T\left(\frac{\cos(Z)}{\cos(i)}\right) \tag{6}$$

This form of cosine correction might be effective for illumination transformations of remotely sensed data in flat terrain, but it is not suitable for the slope-aspect correction problem in practice. It is clear that the simple cosine function inadequately represents the physical situation for large incident angle which gives rise to "over-corrected" effects. This means the corrected image becomes very bright in those places where illumination is nearly grazing the slope terrain since the cosine correction factor, $\left(\frac{\cos(Z)}{\cos(i)}\right)$, becomes quite large or even infinite as the incident angle, i, approaching 90^{o}.

Consequently, considerations must be given to non-Lambertian models, which take into account both diffuse and directional scattering from surfaces. Teillet et al. (1982) adopted four non-Lambertian correction functions (namely, viewer foreshortening, Minnaert, semi-empirical cosine, and diffuse and specular functions) and developed the classification software implementing these functions for both LANDSAT and airborne MSS images. Maximum likelihood classifications for original and slope-aspect corrected data were conducted. Their results show that the slope-aspect corrected data yield no significant improvement in overall classification accuracy over the results obtained using uncorrected data. As many researchers realized, the behavior of LANDSAT data as a function of incidence angle is class-dependent and therefore no specific correction formula is sufficiently general to accommodate the various forest types in mountainous environment (Holben and Justice, 1979; Smith et al., 1980; Justice et al., 1981; Hugli and Frei, 1981; Teillet et al., 1982; Hugli at al., 1983; Woodham and Lee, 1985; Teillet, 1986; and Woodham and Gray, 1987). Teillet (1986) gave a comprehensive summary of image correction for radiometric effects in remote sensing and concluded that:

> "not enough work has been done in this area to establish guidelines on the relative importance of slope-aspect effects on image radiometry for different regimes of terrain relief, cover types and canopy structure characteristics. Thus, while corrections for illumination, viewing angle and atmospheric effects should be applied routinely, radiometric corrections for topography remain experimental and should be used with caution."

The possibility of using terrain variables such as elevation, slope, aspect, and effective incidence angle as additional channels in a feature space was also tested in CCRS. Only elevation data which can approximate a normal distribution as required by the maximum likelihood classification algorithm were selected as best additional variable and added to MSS bands. The classification results were slightly improved for LANDSAT MSS data, but not for airborne MSS data with higher spatial resolution (Teillet et al., 1982).

No discussions were found addressing the spatial point-to-point matching between TM pixels and DEM grids. It is felt that such correspondence should exist for slope-aspect correction with either correction functions described above or adding terrain variables to LANDSAT TM data.

Chapter 3

Study Areas and Data

3.1 Study Area Selection and Location

The Thunderhead Mountain 7.5' U.S. Geological Survey (USGS) quadrangle was chosen as a general study area within the Great Smoky Mountain National Park because both remotely sensed data and digital elevation model (DEM) data with the same ground resolution were available.

Two test areas, Rocky Top and Sugartree Gap, were considered for this study (Figure 3). They were chosen along the mountain ridge across the whole quadrangle from east to west. Figure 4 and 5 are the gray tone representations of digital elevation data produced by the modifications of the over-striking subroutine (Gonzalez, 1987). Rectangular test areas 2 km by 3 km were used because of computational limitations such as computer storage space, the capabilities of displaying results, and the convenience of data manipulation.

The vegetation on the Rocky Top test site is a mixture of northern hardwood forest on the south aspect and cove hardwood forest on the north aspect. The vegetation at the Sugartree Gap area is composed of northern hardwood, cove hardwood, and mesic oak

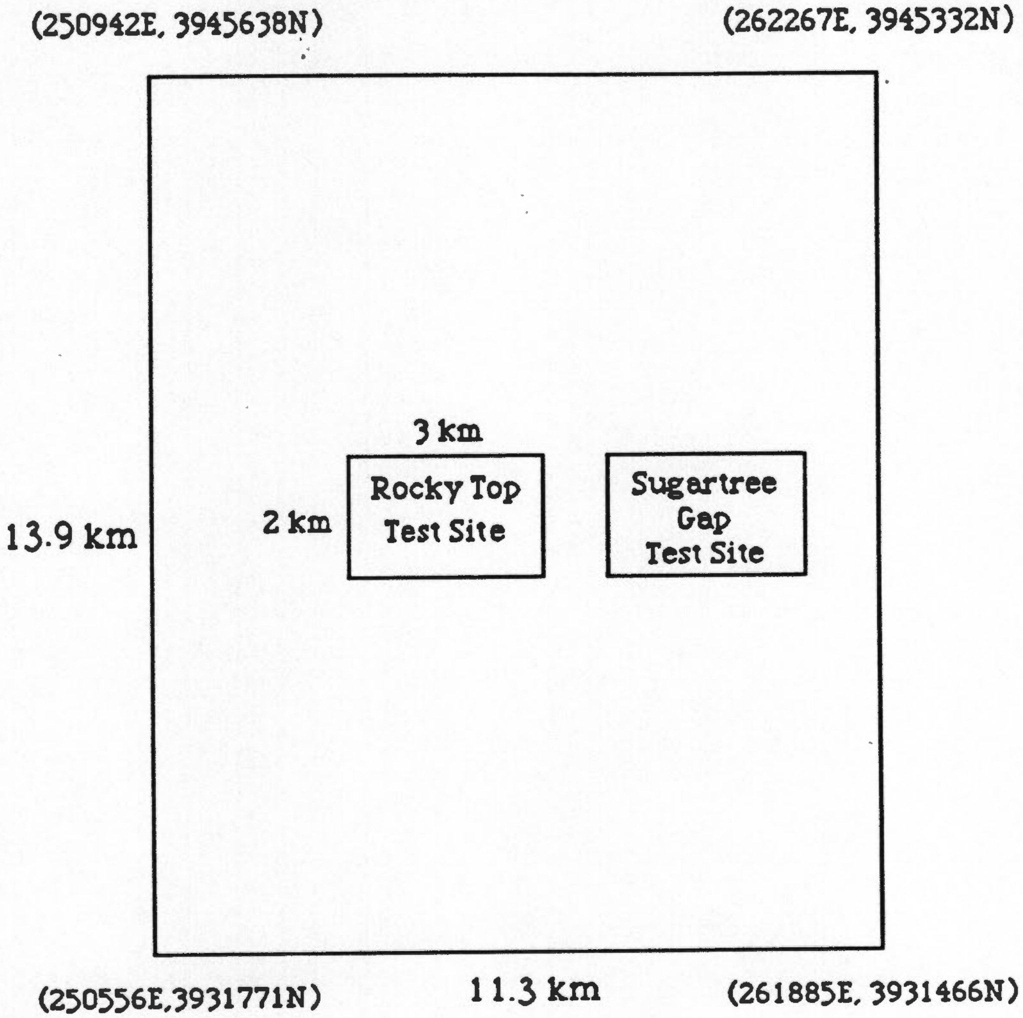

Figure 3. Locations of the two test sites in Thunderhead Mountain Quadrangle with UTM coordinates of quadrangle corners.

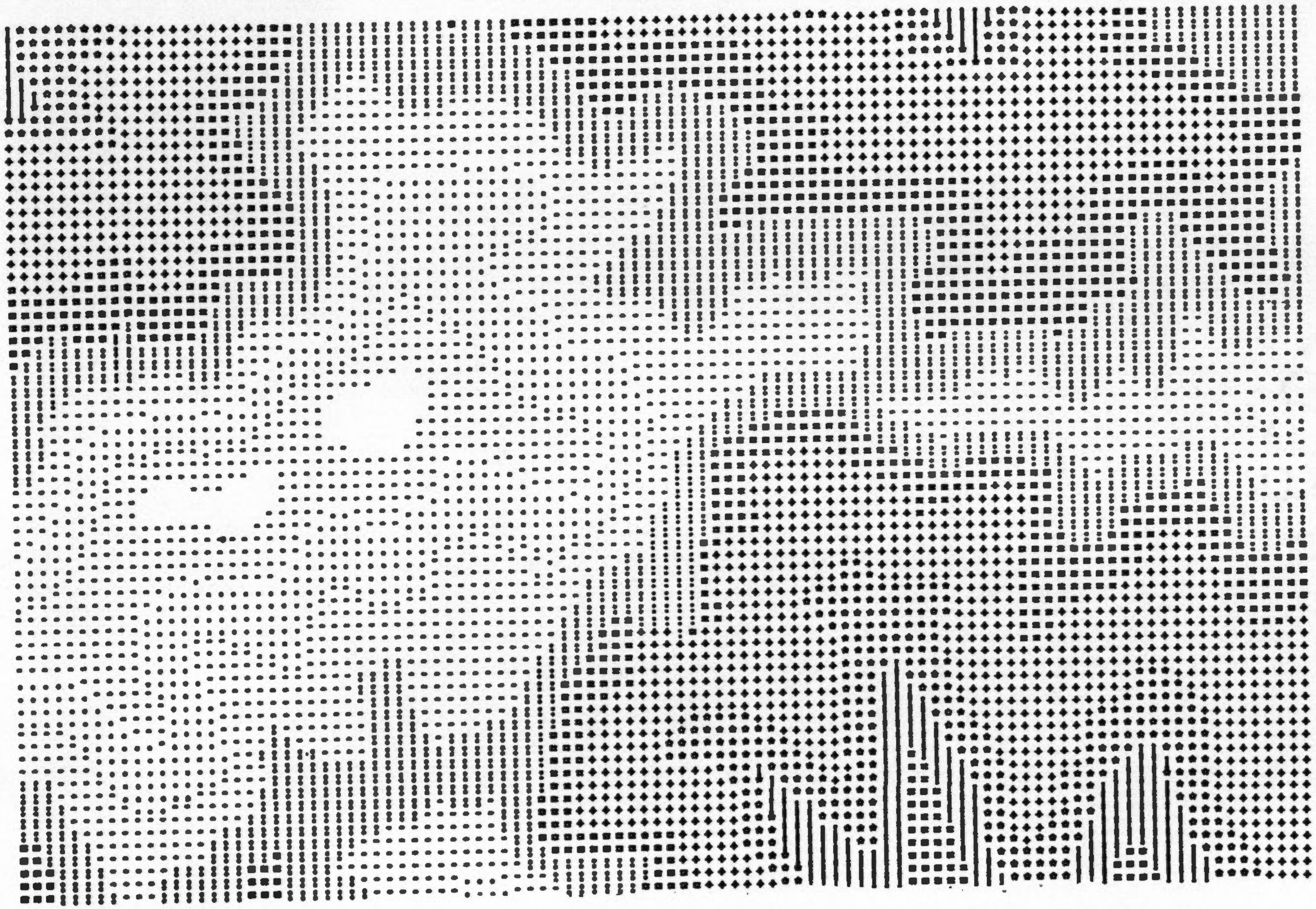

Figure 4. Gray-scale representations of the digital elevation data for the Rocky Top test site (dark regions represent low elevation, and light regions represent high elevation).

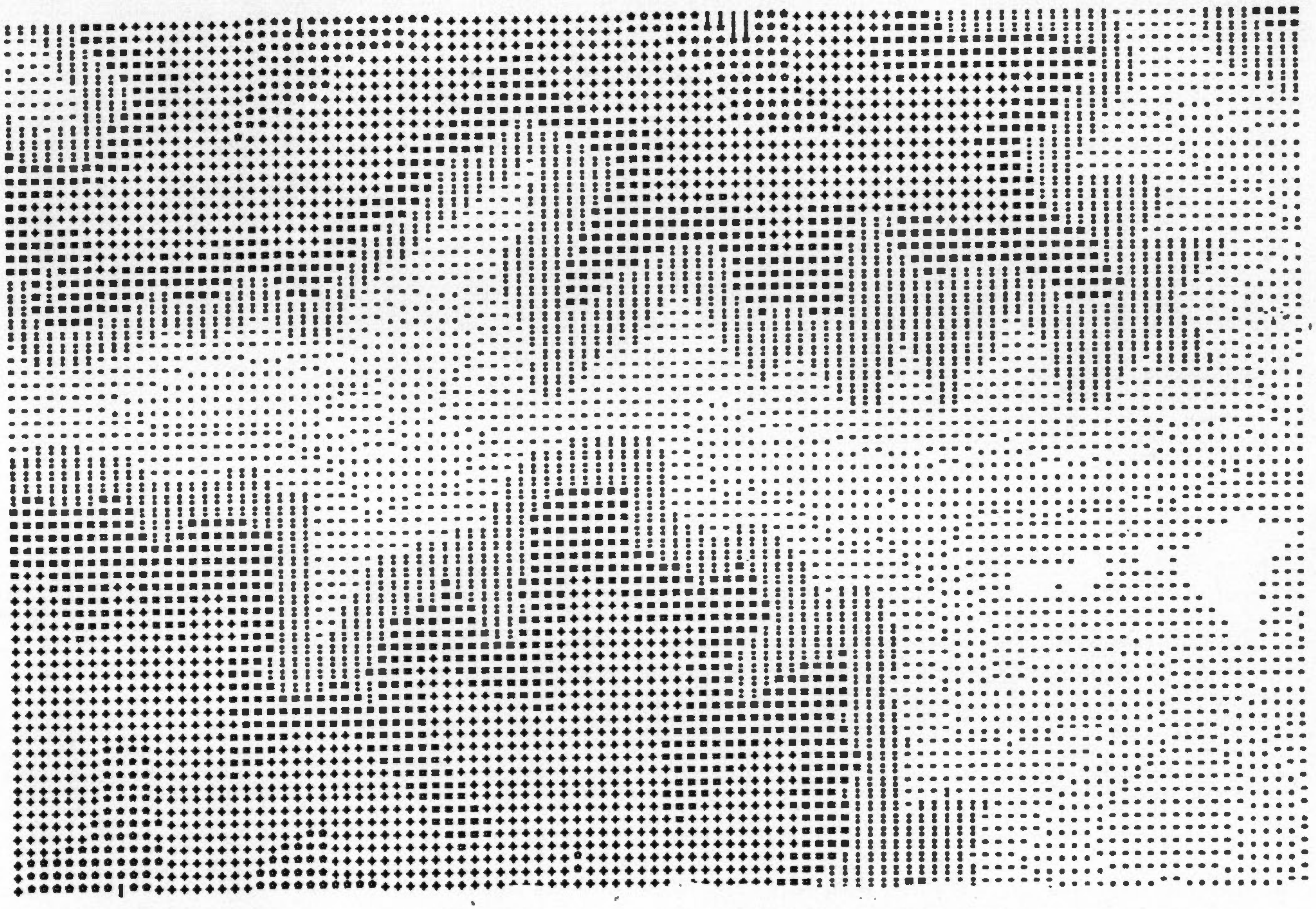

Figure 5. Gray-scale representations of the digital elevation data for the Sugartree Gap test site (dark regions represent low elevation, and light regions represnet high elevation).

(MacKenzie, 1988b). The areas have rugged terrain with elevation varying from about 700 to 1,600 meters above the sea level. Figures 6 and 7 are the contour maps of Rocky Top and Sugartree Gap test sites. They were generated from digital elevation models using the program Surface II to provide the overview of the topographic conditions in these two test areas.

3.2 Data Used for Analysis

3.21 LANDSAT-4 Thematic Mapper (TM) Image

The remotely sensed data for the test sites are LANDSAT-4 Thematic Mapper (TM) digital imagery taken at Greenwich Mean Time 15:42 on September 8, 1984. The Sun elevation angle was 50° and the Sun azimuth angle was 133°. The TM data were georeferenced at a 30 m by 30 m pixel size to the Universal Transverse Mecator (UTM) coordinate system using Earth Resource Data Analysis System (ERDAS) (MacKenzie, 1988a).

The TM is a scanning optical-mechanical sensor system that records reflected and emitted radiation in the visible, reflective-infrared, middle-infrared, and thermal-infrared regions of the electromagnetic spectrum. It collects multispectral imagery that has higher spatial, spectral, and radiometric resolution than the LANDSAT Multispectral Scanner (MSS). LANDSAT TM data have a

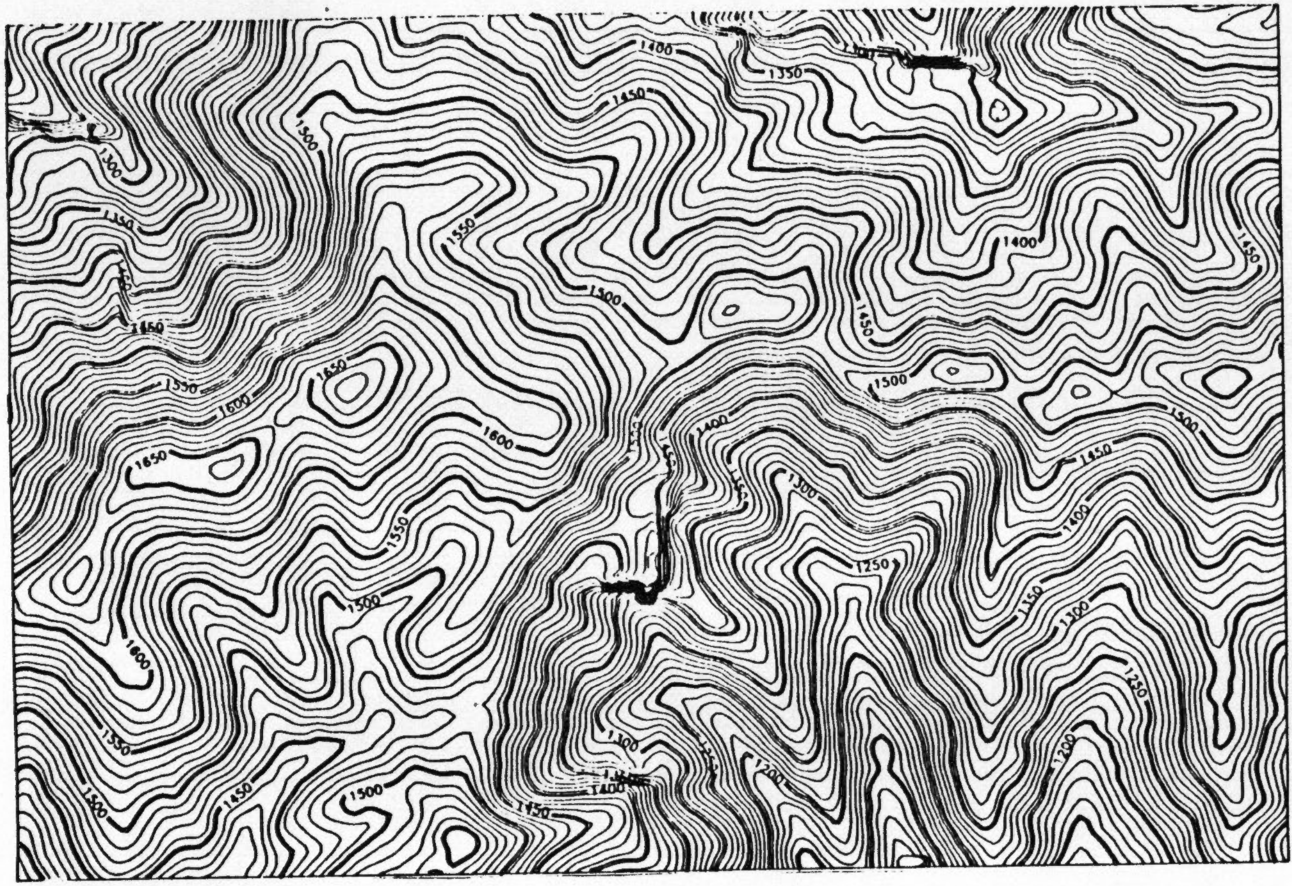

Figure 6. Contour map of the Rocky Top test site created from a digital elevation model (DEM) with 30 m grid.

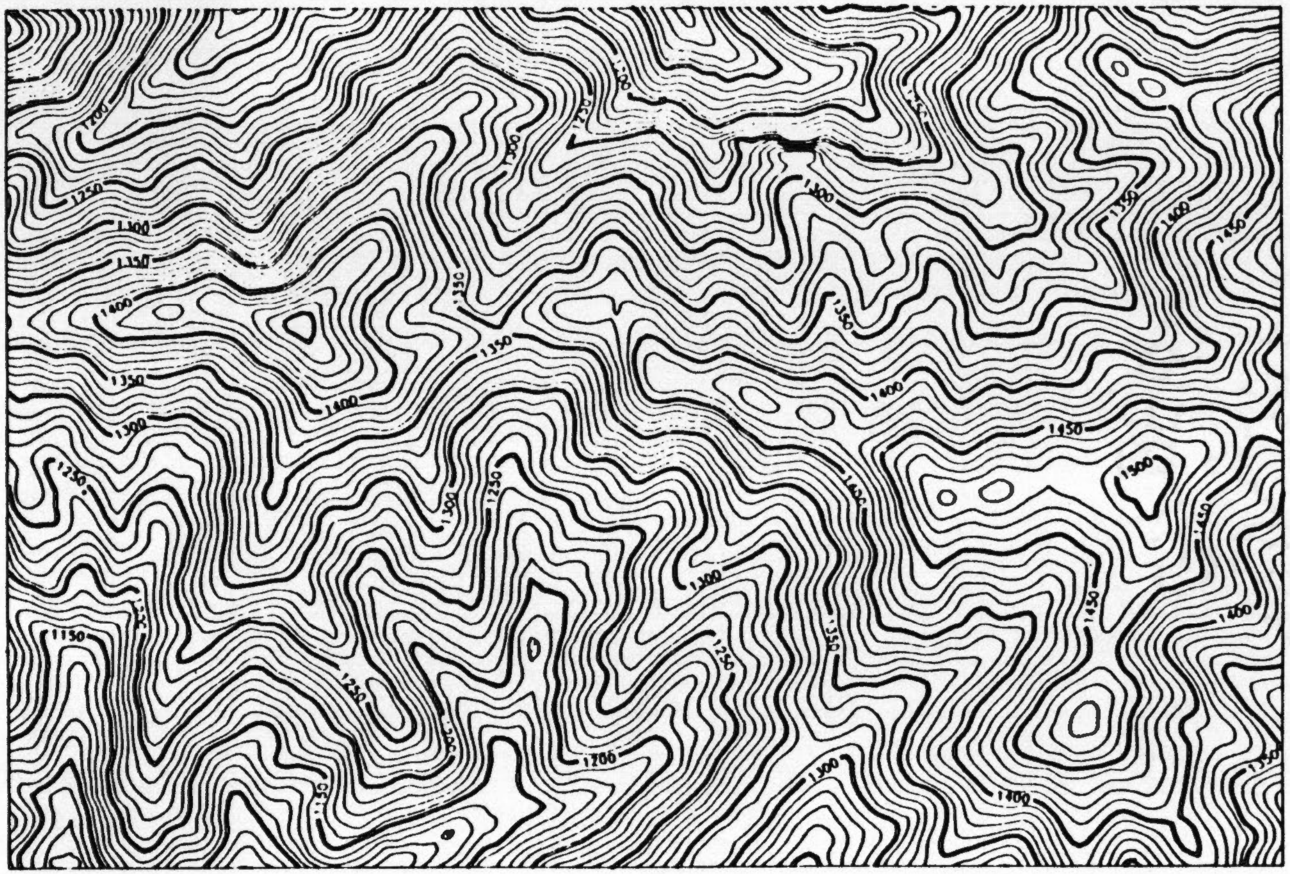

Figure 7. Contour map of the Sugartree Gap test site created from a digital elevation model (DEM) with 30 m grid.

ground projected instantaneous-field-of view (IFOV) of 30 m by 30 m which allows classification accuracies acceptable for most remote sensing applications in agriculture and forestry. Table 1 shows the major features of TM imagery. The TM spectral bands represent important departures from the bands found on the MSS also carried on LANDSAT 4 and 5. The original MSS bandwidths were selected based on their utility for general vegetation inventories and general geologic studies; most of the TM bands were chosen after years of analysis for their value in the discrimination of vegetation type and vigor, plant and soil moisture measurement, differentiation of clouds and snow. Table 2 lists the characteristics of the TM spectral bands.

In this experiment, all seven TM bands were used to examine the effects of topography; the one having the best fit with the synthetic image was chosen to register two different data sets.

3.2.2 Digital Elevation Model (DEM)

The digital terrain data used for this study was a 30 m by 30m digital elevation model (DEM) for the 1:24,000 Thunderhead Mtn. quadrangle and available from the U.S. Geological Survey. This model is an array of terrain elevations on a regular grid, called the planar format. Grid points are projected in UTM coordinates. This DEM was created with the Gestalt Photomapper II and was classified

Table 1. Characteristics of the LANDSAT thematic mapper sensor system (Jensen, 1986)

Band Number	Bandwidth (micrometers)	Instantaneous field-of-view (meters)	Radiometric Sensitivity[1] (NEΔP)
1	0.45-0.52	30 * 30	0.8
2	0.52-0.60	30 * 30	0.5
3	0.63-0.69	30 * 30	0.5
4	0.76-0.90	30 * 30	0.5
5	1.55-1.75	30 * 30	1.0
6	10.4-12.50	120 * 120	0.5 (NEΔT)
7	2.08-2.35	30 * 30	2.4

Data rate:	85MB/s
Quantization levels:	8 bits, 256 levels
Earth coverage:	16 days
Altitude:	705 km

---

1. The radiometric sensitivities are the noise-equivalent reflectance differences for the reflective channels expressed as percentages (NEΔP) and temperature differences for the thermal infrared bands (NEΔT).

Table 2: The Characteristics of LANDSAT TM Spectral Bands (Jensen, 1986)

Bands	Descriptions of Characteristics
Band 1:. 0.45-0.52 µm	This band provides increased penetration of water bodies as well as supporting land use, soil, and vegetation features.
Band 2: 0.52-0.60 µm	This band spans the region between the blue and red chlorophyll bands and therefore corresponds to the green reflectance of healthy vegetation.
Band 3: 0.63-0.69 µm	This is the red chlorophyll absorption band of healthy green vegetation and represents one of the most important bands for vegetation discrimination. It is also useful for soil and geological boundary delineations.
Band 4: 0.76-0.90 µm	This band is especially responsive to the amount of vegetation biomass present in a scene. It is useful for crop identification and emphasizes soil-crop and land-water contrasts.
Band 5: 1.55-1.75 µm	This band is sensitive to the turgidity, i.e., the amount of water in plants. In addition, this is one of the few bands that can be used to discriminate among clouds, snow, and ice.
Band 6: 10.4-12.5 µm	This band is an important band for the discrimination of geologic rock formations.
Band 7: 2.08-2.35 µm	This band measures the amount of infrared radiant flux emitted from surfaces. It is useful for locating geothermal activity, thermal inertia mapping for geologic investigations, vegetation stress analysis, and soil moisture studies.

accuracy level 1 - the lowest class (U.S.G.S., 1987). In this study, small local errors were found in the DEM.

In a Cartesian coordinate system, such as used in the planar case, the x-axis pointing east, the y-axis pointing north and the z-axis perpendicular to the Earth's surface, the digital elevation model can be written explicitly as a function:

$$z = f(x, y) \tag{7}$$

The digital elevation data are usually produced from stereoscopic aerial photographs using suitable photogrammetric instruments. Since the digital elevation model represents a topographic surface in terms of a set of spatial coordinates determined by sampling the surface, the question of the quality of this representation is of interest for evaluating the accuracy of the derived quantities, such as slope and aspect. How accurately a topographic surface is represented by a DEM depends essentially on three factors: the sampling density, i.e., the interval at which elevation is measured in relation to the variability of the surface; the measuring error introduced by sampling a continuous quantity and converting it into digital form; and the interpolation method employed for generating a continuous surface from the discrete data.

The vertical accuracy of the DEM data is dependant on the spatial resolution, quality of the source data, collection and processing procedures, and so forth (U.S.G.S., 1987). When incorporating this model into another spatial data set, the accuracy of geometrical location seems to be of more concerned. The quantitative analysis for the accurate estimation of digital terrain model has been conducted in some research field (Tempfli, 1980). In this study, however, only visual examine of the similarity of the contour map generated from DEM with the U.S.G.S. topographic map was used.

Chapter 4

Methods and Procedures

This chapter will primarily describe the methods and procedures used to realize the objectives addressed before. However, some results are included because they determined subsequent methods.

4.1 Simulating the Topography

4.1.1 Shaded-relief Image Technique

The techniques of "shaded-relief" or "hill-shading" have been used in cartography for many years to produce the illusion of a three-dimensional relief maps (Yoeli, 1967; Peucker el at., 1973; Batson el at., 1975; Schachter, 1980). Since their tonal variation is unambiguously identified with relief and aspect rather than the albedo variation due to cover types, shaded-relief maps are also useful in geology and landscape architecture. They convey an impression of the shape of the landform under a certain illumination condition.

Using elevation data and a model of surface reflectance, the appearance of a scene for any sun angle and viewing angle can be simulated. The resulting synthetic image might be used to predict properties of remotely sensed images.

The principle of a shaded-relief image is that the reflectance of a surface can be expressed as a function of the incident angle (*i*), which allows observed brightness to be related directly to surface orientation (see Figure 1, page 1). In this study, two reflectance models are used to simulate topographic effects: one for a Lambertian reflector and a second for more complex reflector.

The first model is the simple, idealized reflectance model for a Lambertian reflector expressed as:

$$S(i) = u * \cos(i) \tag{8}$$

where: $S(i)$ = synthetic brightness for incident angle i

u = reflectance factor.

This reflectance model describes a surface as a perfect diffuser, appearing equally bright from all viewing directions. The cosine of the incident angle (*i*) accounts for the foreshortening of the surface element as seen from the light source (Smith et al., 1980).

The second model, developed by Lommel in 1888 and modified by Seeliger in the same year, is based on the photometric analysis of rocky planets and satellites (Horn, 1981; Dave and Bernstein, 1982). It describes a surface which reflects varying amounts of light in all direction; the viewing angle (e) is taken into account as shown in equation (9):

$$S(i, e) = \frac{u}{1 + \frac{\cos(e)}{\cos(i)}} \tag{9}$$

To simplify the computation of the synthetic image, a coordinate system is established with the origin at the upper left corner of a digital elevation model (DEM) matrix. The x-axis points to south and the y-axis points east, both parallel to the UTM coordinate grid. Thus the directional slope vectors $\bar{a_x}$ and $\bar{a_y}$ at (x, y) are:

$$\bar{a_x} = (1, 0, p)\,dx \tag{10}$$

$$\bar{a_y} = (0, 1, q)\,dy \tag{11}$$

here dx = dy = 30 meters; p and q are the surface gradients obtained by the partial derivatives of the elevation z with respect to x and y, that is:

$$p = \frac{dz}{dx}, \qquad q = \frac{dz}{dy} \tag{12}$$

The local surface normal vector $\bar{n}$ at (x, y) is then expressed in terms of the cross-product of vectors $\bar{a_x}$ and $\bar{a_y}$ by equation (13):

$$\bar{n} = \bar{a}_x \times \bar{a}_y = dx * dy \begin{pmatrix} \bar{i} & \bar{j} & \bar{k} \\ 1 & 0 & p \\ 0 & 1 & q \end{pmatrix} = (-p, -q, 1)\ dx\ dy \qquad (13)$$

To generate synthetic images including the shading effects at different times, parameters for solar azimuth, ø, and elevation angle, œ, as well as viewer location are chosen to correspond to those of real images. The unit vector $\bar{s}$ in the solar illumination direction (see Figure 8) is given by the following equation :

$$\bar{s} = [\ \cos(\text{ø}) \cos(\text{œ}),\ \sin(\text{ø}) \cos(\text{œ}),\ \sin(\text{œ})\ ] \qquad (14)$$

This can be expressed as the gradient components:

$$\bar{s} = (-p_s\ ,\ -q_s\ ,\ 1) \sin(\text{œ}) \qquad (15)$$

where:

$$p_s = \cos(\text{ø})\ \mathrm{ctg}(\text{œ}) \qquad (16)$$

$$q_s = -\ \sin(\text{ø})\ \mathrm{ctg}(\text{œ}) \qquad (17)$$

The test sites are small enough in area that (p_s, q_s), the vector components in x and y of the solar beam, can be considered as constant throughout both areas.

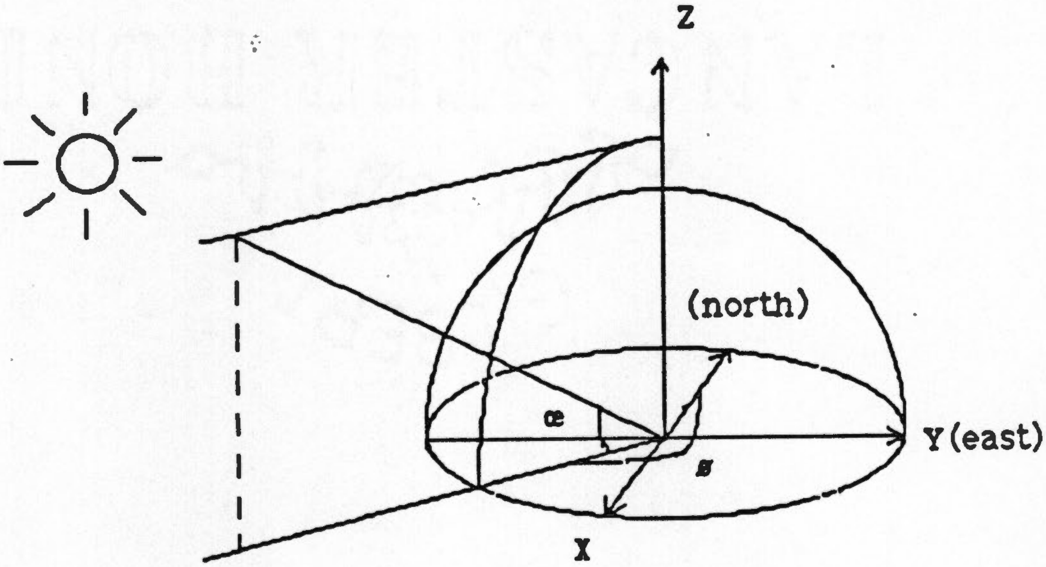

where: œ = the sun elevation angle
ø = the sun azimuth angle
X = X axis pointing to south
Y = Y axis pointing to east
Z = Z axis point to Zenith

Figure 8. The solar direction in an Earth centered coordinate system.

The cosine of an incident angle can be expressed as the dot-product of two vectors, the surface element normal vector $\bar{n}$ and the light source direction vector $\bar{s}$:

$$\cos(i) = \frac{\bar{n} \quad \bar{s}}{|\,\bar{n}\,| * |\,\bar{s}\,|} \tag{18}$$

Similarly, the cosine of a viewing angle is obtained by the dot-product of the normal $\bar{n}$ and the viewing direction vector $\bar{v}$:

$$\cos(v) = \frac{\bar{n} \quad \bar{v}}{|\,\bar{n}\,| * |\,\bar{v}\,|} \tag{19}$$

Since data from satellite-based thematic mapper sensors are considered as a vertical projection, the viewing direction is expressed as:

$$\bar{v} = (0, 0, 1) \tag{20}$$

Thus, the synthetic brightness value based on the two reflectance models are:

$$S_{Lambert} = \frac{u * (p_s*p + q_s*q +1)}{\sqrt{1+p^2+q^2} * \sqrt{1+p_s^2+q_s^2}} \tag{21}$$

$$S_{\text{Lommel-Seeliger}} = \frac{u * (p_s*p + q_s*q + 1)}{(p_s*p+q_s*q+1) + \sqrt{1+p^2+q^2}} \tag{22}$$

In this case the scaler u is chosen as 255 to correspond to the TM data quantitized to 8 bits with a range of values from 0 to 255.

The functions S(p, q) are referred to as reflectance map and determine scene radiance as a function of p and q (Horn, 1977). Reflectance maps provide a general viewer-centered representation for specifying the surface reflectance of a material for a particular light source, surface and viewer geometry.

4.1.2 Gradient Estimation

As indicated in (20) and (21), the apparent brightness of a surface element depends on its orientation to the viewer and to the light source. The orientation of the surface element is fully described by a surface normal, or equivalently by the gradient. In the areas where digital elevation data are available, the components of the gradient (p, q) can be estimated from the matrix of terrain elevation with gradient algorithms.

The most frequently used gradient algorithm in digital image processing is referred to as the Sobel gradient operators. They involve 8-neighborhood pixels about point (x, y). That is:

$$\left.\begin{aligned}p_9&=[(Z_{x+1,y-1}+2Z_{x+1,y}+Z_{x+1,y+1})-(Z_{x-1,y-1}+2Z_{x-1,y}+Z_{x-1,y+1})]/(8dx)\\ q_9&=[(Z_{x-1,y+1}+2Z_{x,y+1}+Z_{x+1,y+1})-(Z_{x-1,y-1}+2Z_{x,y-1}+Z_{x+1,y-1})]/(8dx)\end{aligned}\right\} \quad (23)$$

These expressions produce excellent estimates for the components of the gradient of the central point. Using a 3 by 3 pixels subarea in the computation of the gradient has the advantage of increased smoothing over smaller operators, tending to make the derivative operations less sensitive to error induced by the production of digital terrain elevations (Gonzalez, 1987). However, more calculations and storage are required to manipulate terrain data.

For comparison, an algorithm with gradient operators based on four points was used.

$$\left.\begin{aligned}p_4 &= [(Z_{x+1,y+1} + Z_{x+1,y}) - (Z_{x,y+1} + Z_{x,y})] \;/\; (2dx)\\ q_4 &= [(Z_{x+1,y+1} + Z_{x,y+1}) - (Z_{x+1,y} + Z_{x,y})] \;/\; (2dy)\end{aligned}\right\} \qquad (24)$$

Here the average gradient is being estimated in the bottom-right quadrant ($Z_{x,y}$, $Z_{x,y+1}$, $Z_{x+1,y}$, $Z_{x+1,y+1}$) rather than at the central point, using elevations in a 2 by 2 pixels neighborhood only. This algorithm is simpler, but introducing less smoothing. Figure 9 illustrates the elevations in the neighborhood of a particular point estimated in the above two schemes.

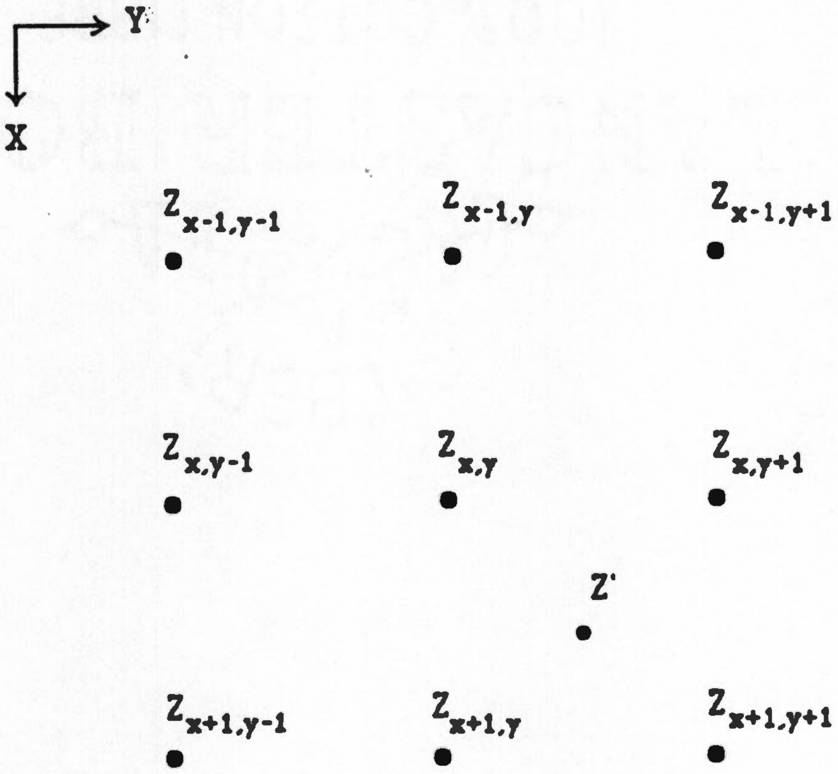

Figure 9. The notation for elevations of neighboring points. Where $Z_{x,y}$ is center with nine point gradient operators and Z' is center with four point gradient operators.

4.2 Registering Two Different Data Sets

4.2.1 Possible Approaches

It is obvious that the wealth of information contained in the digital terrain model can only be used when a one-to-one correspondence can be established by precise superimposition of all image planes, e.g., in a geographic frame.

The standard method to register two images is the reference point approach. First, a spatial transformation is performed; this defines the rearrangement of pixels on the image plane through the use of ground control points. Second, gray levels are interpolated and assigned to pixels in the spatially transformed image (Gonzalez, 1987).

Using the reference point approach to register TM images with synthetic images was unsuccessful in the test areas selected because: (1) there were very few appropriate ground features on the TM image for reference points and (2) corresponding points could not be identified on a synthetic image due to its nature.

A more sophisticated procedure would be to match images indirectly; first, a feature extraction processing would be performed on both the real image and the synthetic image; then, these features would be used to derive the transformation parameters by either similarity measure or Hough transform to register the two images (Little, 1982; Yam and Davis, 1981). It is clear that this approach is limited by (1) the apparent position of a feature being dependent on illumination condition, and (2) the current feature extraction scheme being expensive and complex in computation.

Since both remotely sensed TM image and DEM data for this study are projected in the UTM coordinate system and also share the same size of pixel grid, no further rotation, scaling transformation are needed. The method used here had two steps. First, qualitative matching for Sugartree Gap test site was done through visual comparison of the gray tone image of the TM band 4 reflectance with that of the synthetic brightness generated from DEM based on the Lambertian model. Secondly, quantitative registering was achieved by similarity measure (image cross-correlation) and statistical correlation. The results (translating parameters) from the first test site were then applied to the second test site, Rocky Top, to evaluate the procedures.

4.2.2 Visual Method

Gray tone images of the Sugartree Gap test site based on both the TM band 4 (TM4) spectral reflectance values and the synthetic brightness values simulating topographic effect with the Lambertian model were used for the visual approach. The gray tone images of LANDSAT TM reflectance corresponded to the region of test site and consisted of 69 by 102 pixels. The DEM matrices used to generate the synthetic brightness were 3 rows longer and 3 columns wider (i.e., 72 by 105 elevation points) than the TM images so that each TM pixel can be correlated with the surrounding 9 synthetic brightness values (Figure 10). The intensity values of gray tone images ranged from 0 to 31 which produced by over-striking techniques with an HP LaserJet Printer.

In the procedures of registration, the gray tone image of TM4 reflectance was utilized as a reference image and synthetic images were considered as the target images to search for the best match with TM data set.

Figure 11 is the gray tone image of TM4 reflectance of the Sugartree Gap test site with the midpoint UTM coordinate (259491E, 3938992N). The simulated gray tone image of the same area based on the Lambertian synthetic brightness values is shown in Figure 12. This image is centered at (259500E, 3939000N). The presence of shadows and the overall shading of terrain are quite apparent based on comparison of these two figures. Therefore, the gray tone image of the synthetic brightness was overlaid on a gray tone image of TM4.

Visual examination of Sugartree Gap test site indicated that the TM image was shifted about two pixels north and three pixels west from DEM grid in terms of geometrical coordinates. According to the above findings, another synthetic image, based on a DEM matrix of the same size but shifted 90 meters west and 60 meters north, was created. This image is centered at (259410E, 3939060N) UTM

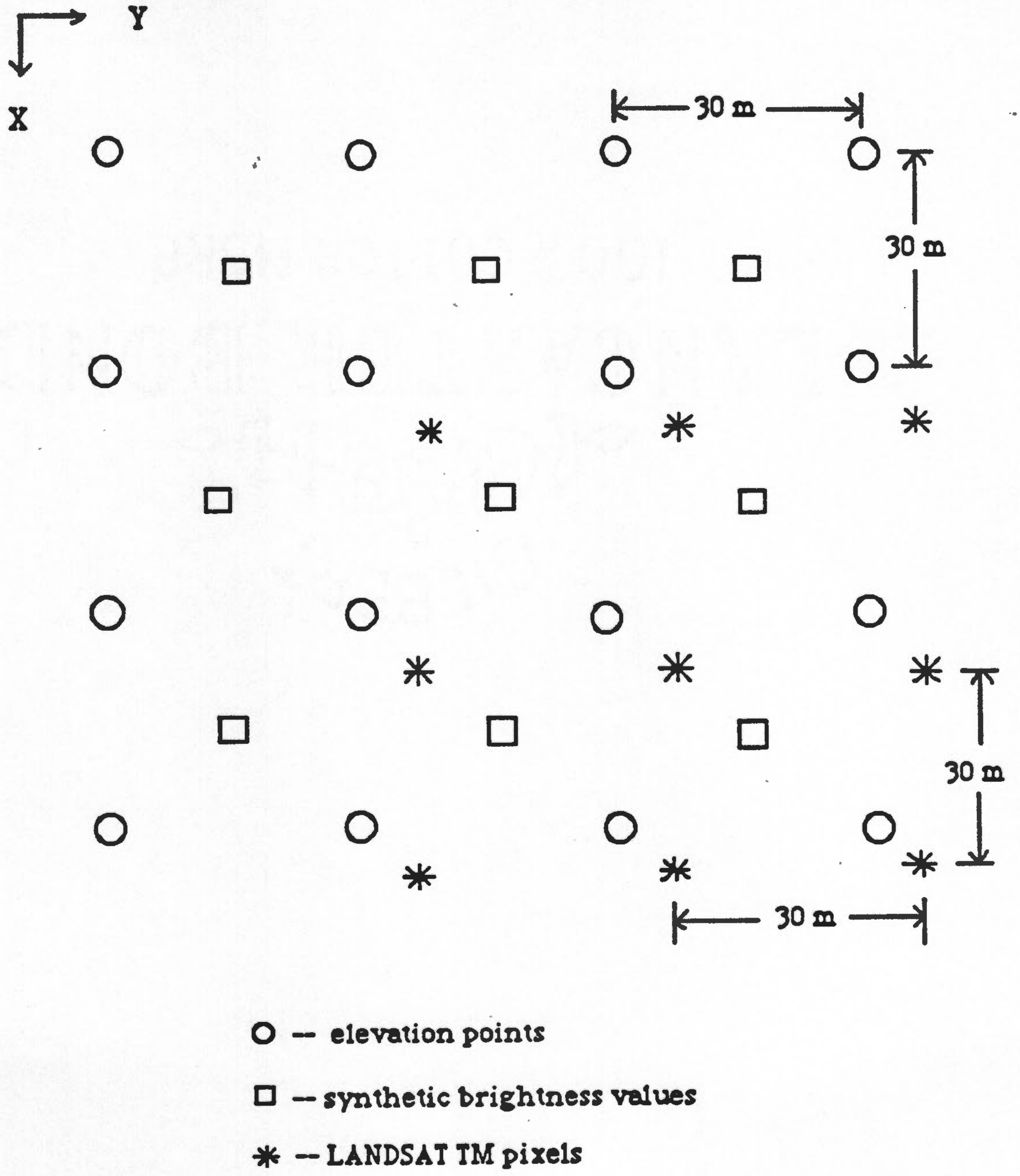

Figure 10. Locations of TM pixels in DEM grid based on UTM frame.

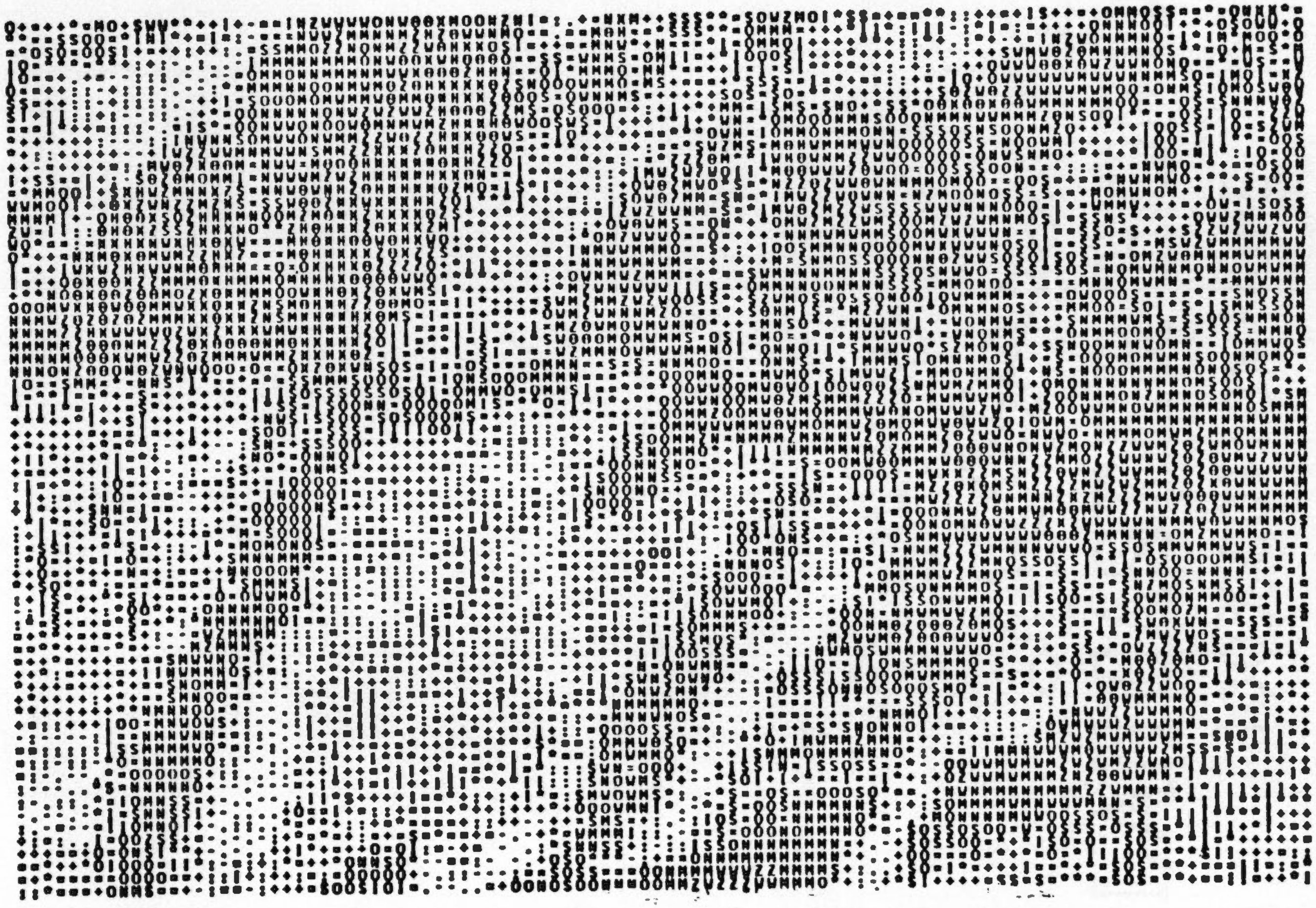

Figure 11. Gray tone image based on LANDSAT TM band 4 reflectance of the Sugartree Gap area.

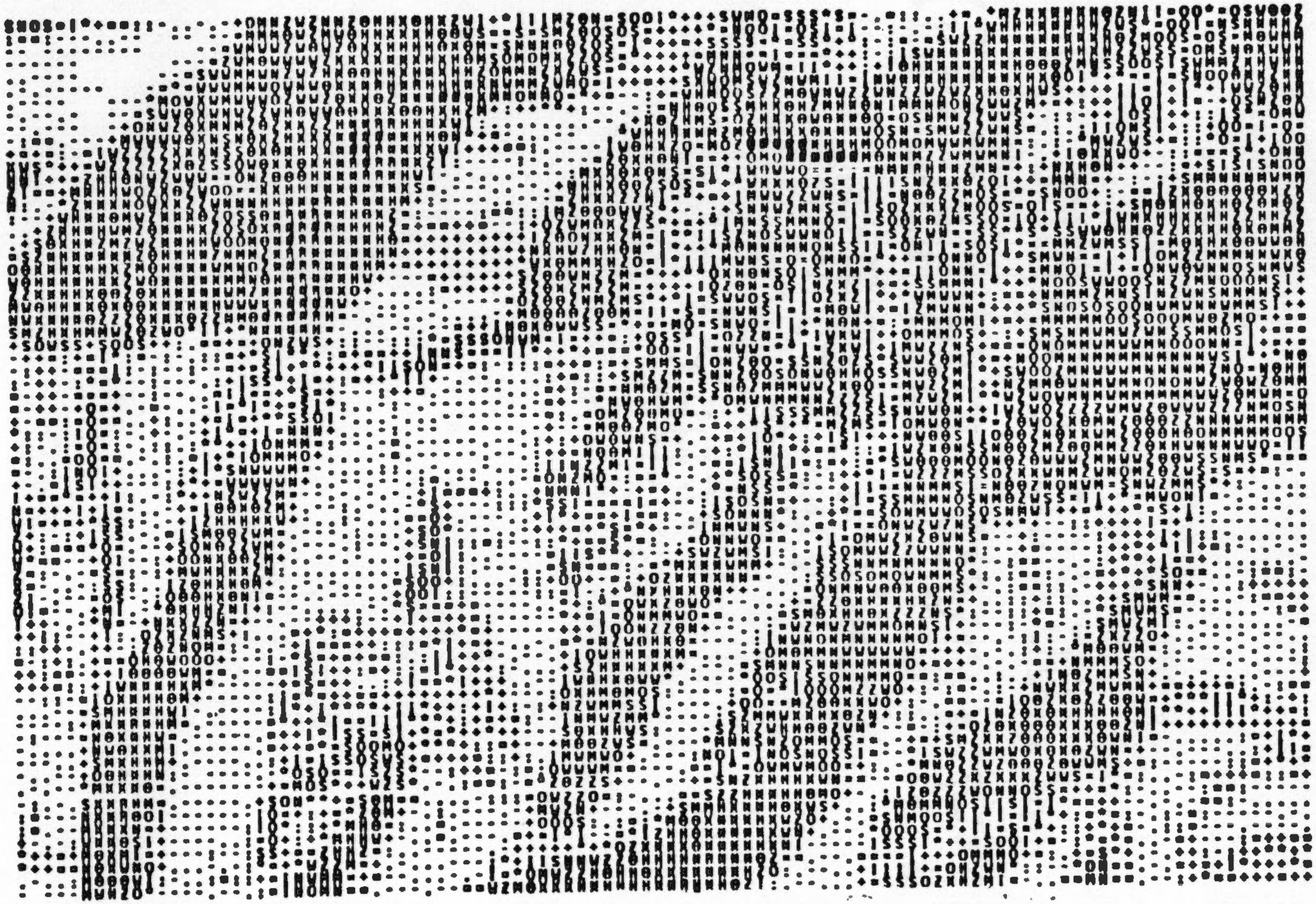

Figure 12. Synthetic image of the Sugartree Gap test site from a DEM with midpoint (259500E, 3939000N) based on the Lambertia model.

coordinate. The gray tone image of the synthetic brightness generated from the new DEM matrix merged quite well with that of the TM4 reflectance within the 69 by 102 image frame based on visual inspection.

4.2.3 Quantitative Analysis

To quantify how closely the synthetic image matches with the TM image, a similarity measure and statistical correlation analysis were performed. The quantitative approach was first carried out to more precisely register DEM to TM data for Sugartree Gap test site and then applied to Rocky Top test site to check the results.

The similarity measure (or image cross-correlation) is based on the similarity of the intensity distribution between the two images to be registered (Rosenfeld, 1982; Horn and Bachman, 1978). Let R(i,j) be the intensity of the real image at the j th picture cell across in the i th row from the top of the image, and define S(x', y') similarly for the synthetic image. The measure of difference between the two images may be obtained by summing the square of the difference:

$$\sum_{i=0}^{M} \sum_{j=0}^{N} [R(i,j)-S(x', y')]^2 \qquad (25)$$

This measure will be minimal for exact alignment of the images. Expanding the formula,

$$\sum \sum R^2 + \sum \sum S^2 - \sum \sum R*S \qquad (26)$$

The first term is the sum of R^2, which is constant, since we always use the the full real image. The second term is the sum of S^2 which should vary slightly as different initial points of synthetic image are chosen. The sum of R*S is most sensitive to the dissimilarity of brightness values between the real image and a synthetic image. This term is called the cross-correlation between two images R and S. By the Cauchy-Schwarz inequality, we can obtain the normalized cross-correlation used as a measure of match:

$$C_{RS}(m,n) = \frac{\sum_{i=0}^{M} \sum_{j=0}^{N} R(i,j)*S(x+m,y+n)}{\left[\sum_{i=0}^{M} \sum_{j=0}^{N} R^2(i,j) * \sum_{i=0}^{M} \sum_{j=0}^{N} S^2(x+m,y+n) \right]^{1/2}} \qquad (27)$$

where: $m = 1, 2, ..., k$; $n = 1, 2, ..., L$.

A perfect match of the two images corresponds to a normalized correlation of one. In this study, $k = L = 3$; that is, values of the similarity measure were calculated for 9 points of each synthetic image with respect to the TM band 4 image. The maximal indicates the number of row and column in which the synthetic image was matched with TM image best. If the maximal value was found at edge of the window, say the first row, then another DEM matrix shifted one row to north would be created. This procedure would be repeated until the maximum similarity value was found at (2, 2), that is at the midpoint of window. Figure 13 shows the results of similarity measure of synthetic images versus TM4 image for Sugartree Gap test site.

The pairs of images with the best match were outputed and linked to Statistical Analysis System Software (SAS) to be analyzed statistically. The TM images were then correlated with the Lambertian synthetic image using the initial point indicated by the maximal value in 3 by 3 measuring window. Figure 13 also presents the values of correlation coefficients calculated for selected similarity measures.

These procedures indicated that the best match was between TM4 image with midpoint (259491E, 3938992N) and DEM data set centered at (259410E, 3939120N). Figure 14 and 15 show the scatter plots for the TM4 image versus the synthetic brightness from both the original and the shifted DEM matrixes. The corresponding correlation coefficients are 0.263 and 0.825, respectively.

These translation parameters of DEM data set shifting from TM image (90 meters east and 120 meters south) were applied to the registration of the Lambertian synthetic and TM4 images for the

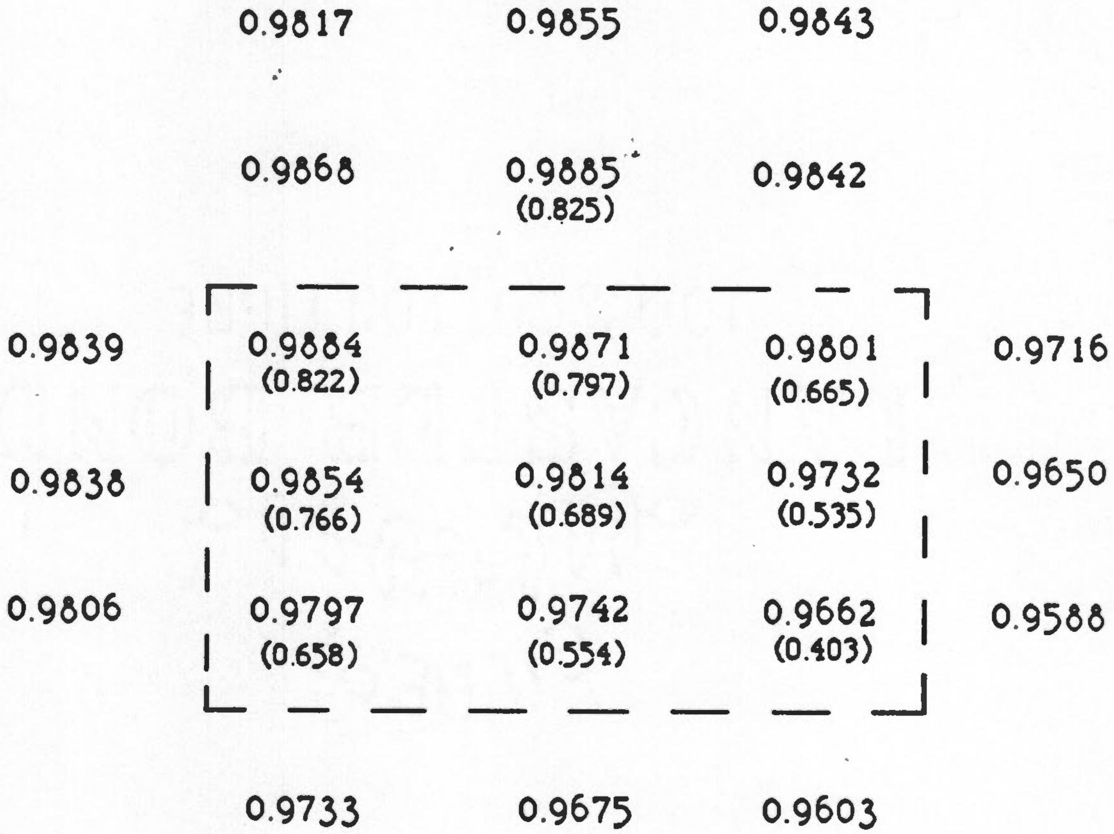

	0.9817	0.9855	0.9843	
	0.9868	0.9885 (0.825)	0.9842	
0.9839	0.9884 (0.822)	0.9871 (0.797)	0.9801 (0.665)	0.9716
0.9838	0.9854 (0.766)	0.9814 (0.689)	0.9732 (0.535)	0.9650
0.9806	0.9797 (0.658)	0.9742 (0.554)	0.9662 (0.403)	0.9588
	0.9733	0.9675	0.9603	

Figure 13. The results of similarity measure of the Lambertian synthetic brightness versus TM4 reflectance for Sugartree Gap test site. (Numbers enclosed with broken line are values of similarity measure for initial 3 * 3 window, while values outside are the those subsequently calculated in search for maximum. Selected correlation coefficients are in parenthesis.)

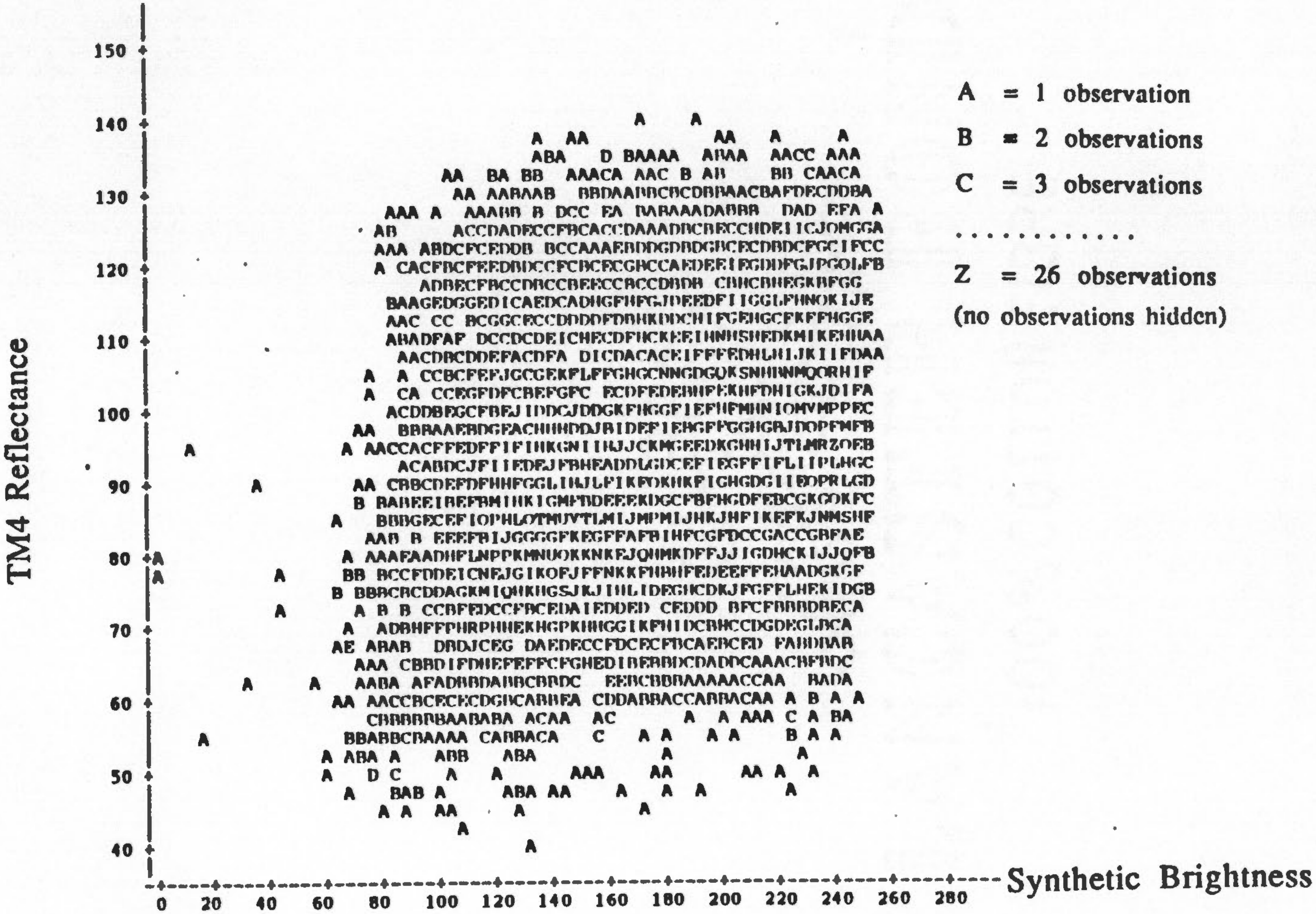

Figure 14. A scatter plot of TM4 reflectance versus the Lambertian synthetic brightness created from a DEM with midpoint at (259500E, 3939000N) UTM coordinate (7038 pixels).

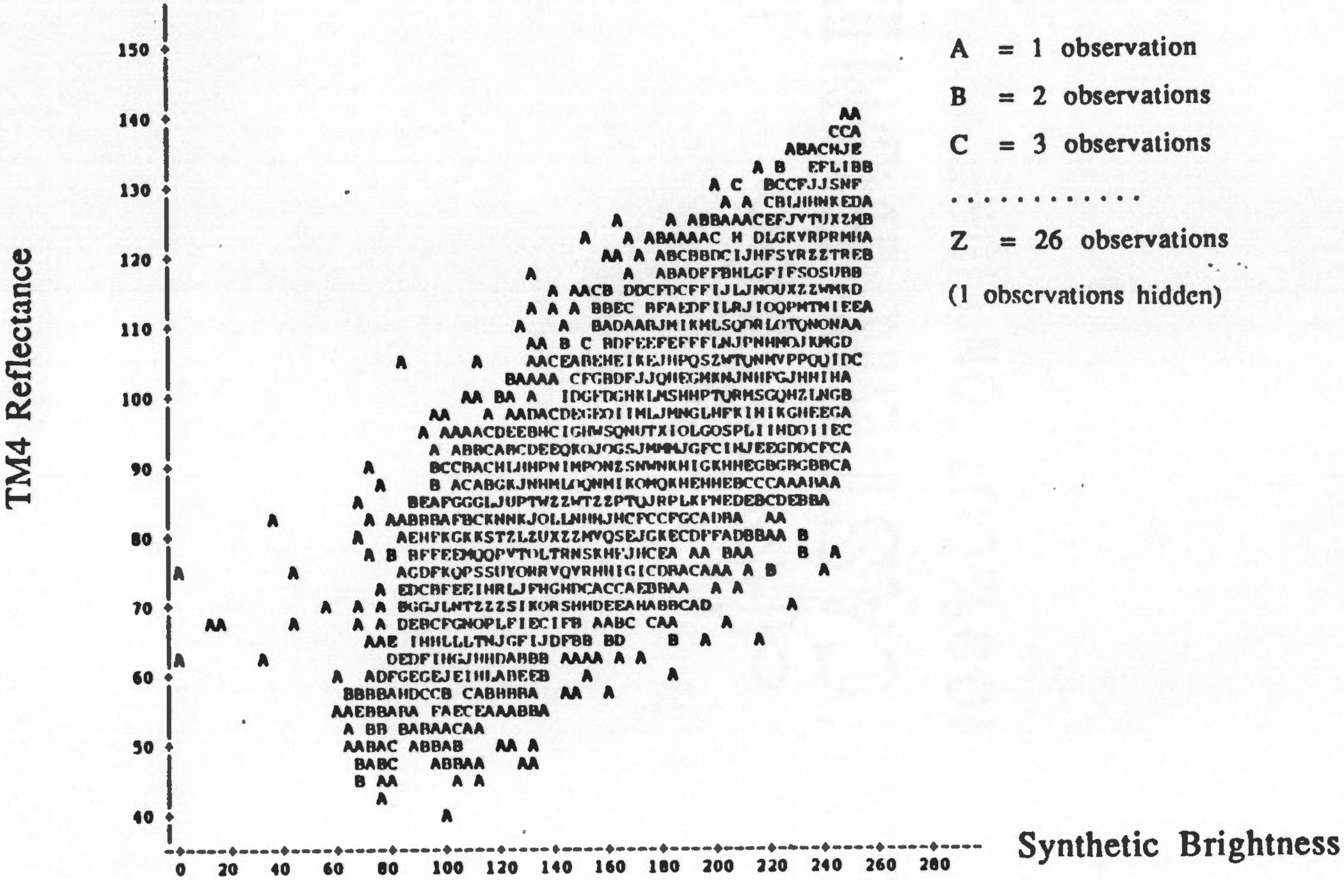

Figure 15. A scatter plot of TM4 reflectance versus the Lambertian synthetic brightness created from a DEM centered at (259410E, 3939120N) UTM coordinate (7038 pixels).

Rocky Top test site; the results for Rocky Top test site were very similar to those with Sugartree Gap test site. Figure 16 is the scatter plots of TM4 image versus the synthetic brightness from Lambertian model; the correlation coefficient is as high as 0.832. The fact that the same translation parameters were found in two separate areas confirms that no visible rotation and scaling errors exist between remotely sensed TM image and digital terrain data set in these test areas.

4.3 Separating Ground Spectral Patterns

4.3.1 The Disparity Between TM Images and Synthetic Images

Since no general method can be effectively utilized to eliminate topographic effects in radiance scenes, another approach was taken based on the linear relationship of TM data and synthetic images. The relation between the remotely sensed image and the synthetic image is not functional since more than one real value occurs for each predicted synthetic brightness. Let T(x, y) stand for the LANDSAT TM image and S(x', y') for the synthetic image. Here the synthetic image predicts brightness values based on either the Lambertian model or the Lommel-Seeliger model. When the Lambertian model is used,

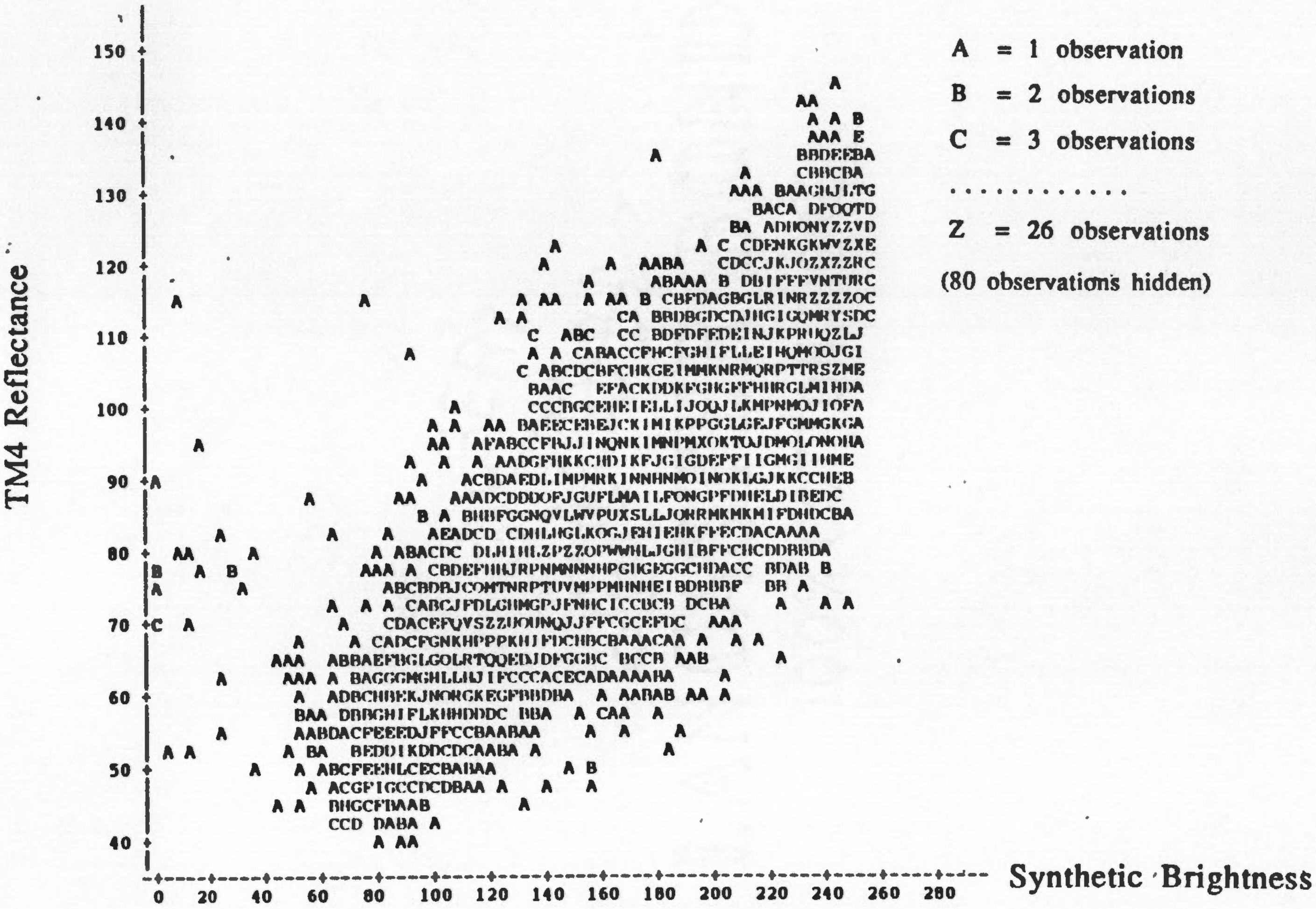

Figure 16. A scatter plot of TM4 reflectance versus the Lambertian synthetic brightness of Rocky Top test site (7038 pixels).

$$S(x', y') = u * \cos(i) \qquad (28)$$

where u = 255. If this were a perfect model, the TM image would be characterized by the equation:

$$T(x, y) = a + b * [u(x, y,) * \cos(i)] \qquad (29)$$

where a and b are estimators introduced to account for atmospheric and sensor parameters, u(x, y) express the dependence of reflectance factor on ground covers (i.e., surface materials). Under the assumption that a and b are constants for all cover types in a single band of remotely sensed image, the LANDSAT TM image should follow the linear relationship with the synthetic brightness as indicated in (29). In other words, a scatter plot of TM image versus synthetic image should cluster about a straight line. Local deviations from that line could be attributed to the local deviations of u(x, y) from the fixed u adopted in (28) (i.e., u = 255).

4.3.2 Creating Residual Image

Based on the above discussion about the disparity between the TM image and synthetic image, the quantitative expression of local deviations from estimated straight line can be expressed in terms of residuals from linear regression between the TM and synthetic images. Thus, the residuals are obtained by simply subtracting the actual TM reflectance by the predicted reflectance as shown in Equation (30):

$$R(x, y) = T(x, y) - \hat{T}(x', y') \tag{30}$$

where the predicted reflectance $\hat{T}$ is given as follows:

$$\hat{T}(x', y') = a + b' * S(x,' y') \tag{31}$$

where: $b' = b * [\frac{u(x,y)}{u}]$

that is, we take the synthetic brightness as a variable to compute the predicted TM reflectance $\hat{T}$ using linear model (Equation 31), then the residuals were constructed as the difference between the actual TM reflectance and the predicted TM reflectance (Equation 30) (SAS manual, 1986). This is accomplished by regressing the actual TM spectral reflectance against the paired reflectance values predicted from the synthetic image. The residuals represent the deviations greater than or less than the expected linear model. The regression and residuals were calculated with SAS.

The distribution of these residuals is typically positive and negative about a residual value of zero. The residuals, therefore, must be adjusted to all positive values for display. Furthermore, an image of these residuals should be able to predict ground spectral patterns directly related to cover types without the interference of local topography.

4.3.3 Segmenting Residual Images

To some extent, a residual image represents the ground spectral patterns in terms of a linear model between effective LANDSAT TM bands and the cosine of solar incident angle. Therefore, segmentation of residual images was conducted to extract spectral features.

The goal of segmentation is to partition an image into its constituent parts or regions, each having a homogeneous property such as intensity, color, texture, etc. (Bhanu, 1987). Thus, the similarity of gray-level values is the basic concept in many segmentation algorithms such as thresholding, edge detection, clustering, region growing, region splitting and merging (Rosenfeld, 1982; Gonzalez, 1987).

Segmentation based on the analysis of the distribution of features is a widely used technique for image segmentation. It makes use of an elaborate peak location and selection procedure, which provides threshold values for the purpose of image segmentation. Gray level thresholding can be easily implemented in an interactive mode with a CRT display and operator-controlled cursor. However, selection of the best threshold level is a difficult task and must usually be associated with a *priori* knowledge about the scene

(Schowengerdt, 1983), because the range of intensities for each spectral pattern will probably overlap with the ranges of others in remotely sensed images of natural scene. As a result of this overlap, the histogram is usually unimodal. Figure 17 illustrates the distribution of residuals and shows the unimodal pattern. Because of the limitation of displaying for this study, the range of residual values has to be compressed to 32 gray-levels, which makes it impossible to select thresholds based on the distribution histograms of residual images (Figure 18).

Thus, in this study two sine criteria (Guo, 1987) were utilized to perform residual image scaling. The first (Equation 31) emphasizes the middle range of the gray-levels and compresses the information in the two ends, and the second (Equation 32) finely distinguishes the high and low ranges of gray-levels but coarsely scales the middle range of the gray-levels. They can be expressed as:

$$Flev_1 = Fl + \frac{(I-1)*(Fh-Fl+1)}{GN} + [0.1*(Fh-Fl)*\sqrt[5]{\frac{1.1}{\sqrt[3]{GN}}} + 0.4]*\sin\frac{2(I-1)\pi}{GN} + 0.5 \tag{32}$$

$$Flev_2 = Fl + \frac{(I-1)*(Fh-Fl+1)}{GN} - [0.1*(Fh-Fl)*\sqrt[5]{\frac{1.1}{\sqrt[3]{GN}}} + 0.4]*\sin\frac{2(I-1)\pi}{GN} + 0.5 \tag{33}$$

where:

$I = 1, 2, 3, \ldots\ldots, GN$

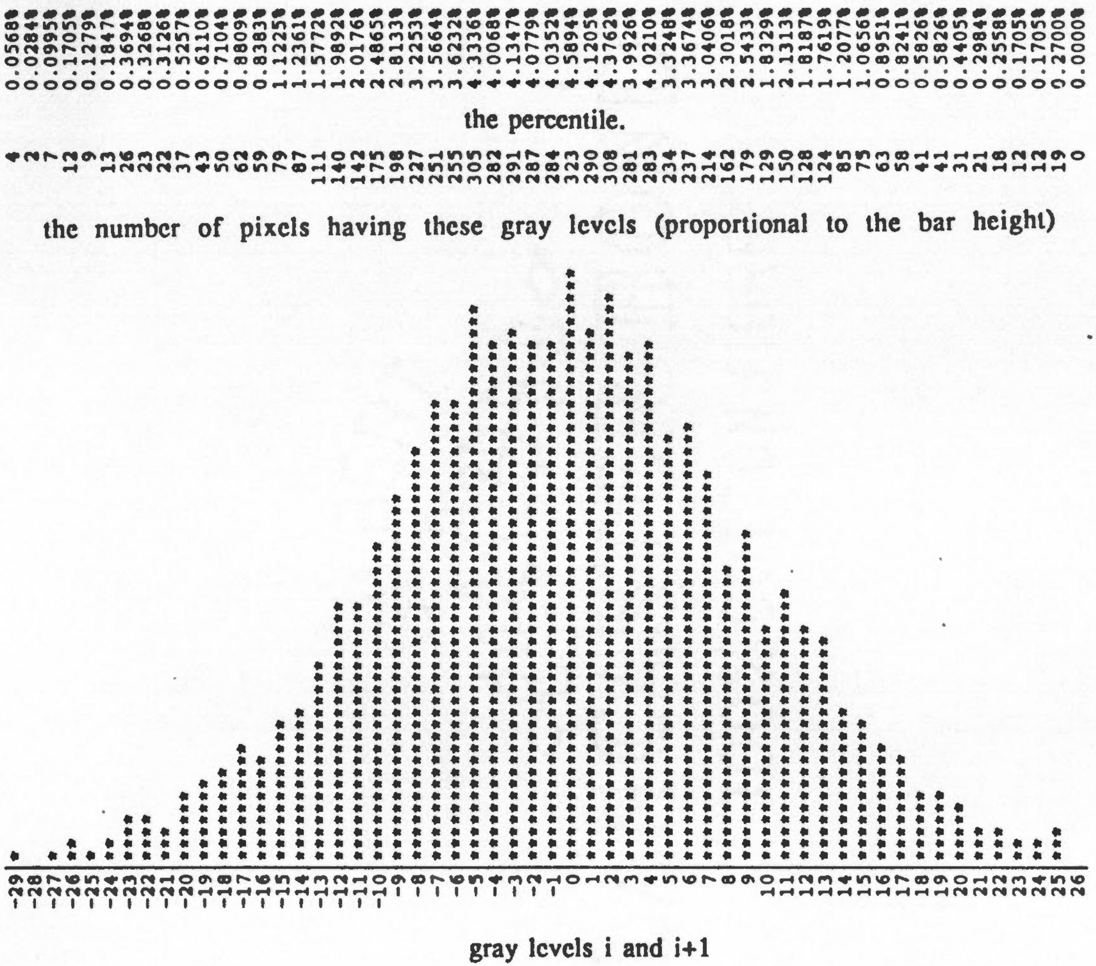

Figure 17. The original gray-level histogram of the intensity distribution of the residual image produced from the linear regression of the Lambertian brightness and TM4 reflectance.

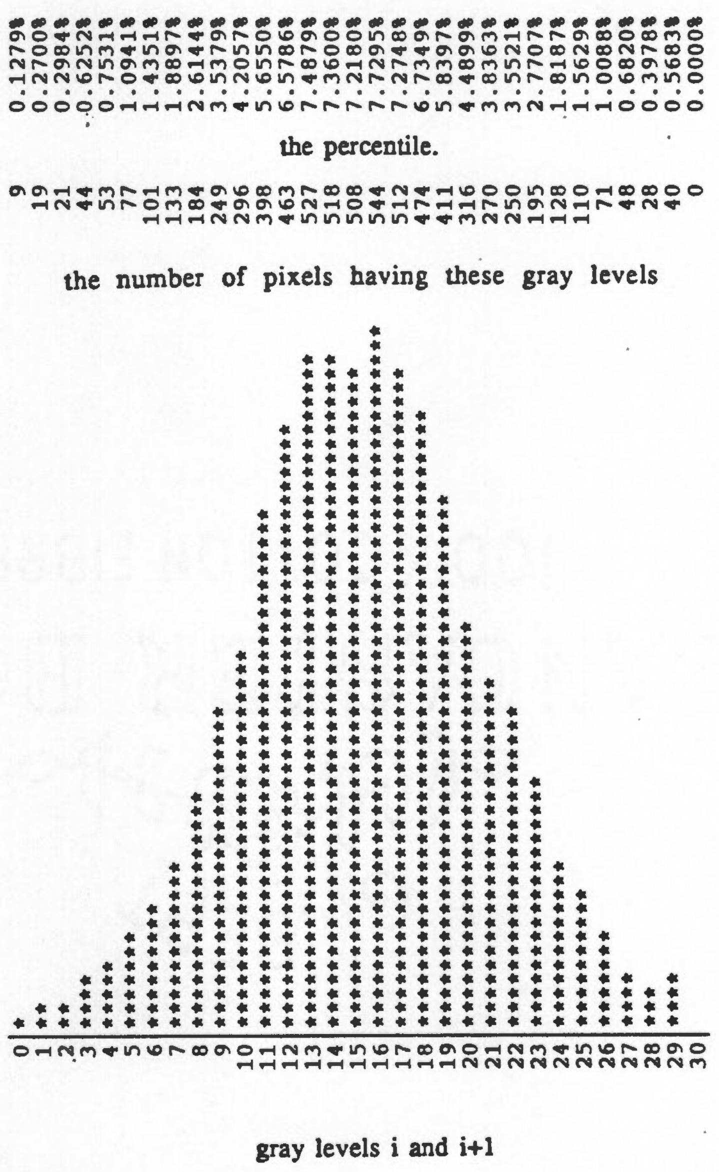

Figure 18. The gray-level histogram of the intensity distribution compressed from the histogram shown in Figure 17.

Flev = segmenting value each level

GN = the number of levels to be segmented

Fh = the maximal of gray-levels

Fl = the minimal of gray-levels

Based on the features of these two segmenting criteria, the residuals close to the value of zero and those dispersed from the value of zero can be effectively extracted and presented.

Chapter 5

Results, Conclusions, and Discussions

This chapter will present the results of the methods described in chapter 4 and give the discussion in three sections. These sections correspond to the three objectives of this study.

5.1 The Topographic Effects in LANDSAT TM Data of Test Areas

5.1.1 Comparisons of LANDSAT TM and Synthetic Images

Visual comparisons of Figures 11 and 19 for Sugartree Gap test site provide a qualitative sense of how well the synthetic brightness represents the LANDSAT TM reflectance. In these images, regions with a dark tone corresponding to those with either low ground albedo values or shadows. Figures 20 and 21 are the gray tone images of TM4 reflectance and synthetic brightness for Rocky Top test site. The presence of shadows and overall shading of terrain is well modeled by each synthetic image. Apparently, the topographic effects dominate in LANDSAT TM images of these two test sites.

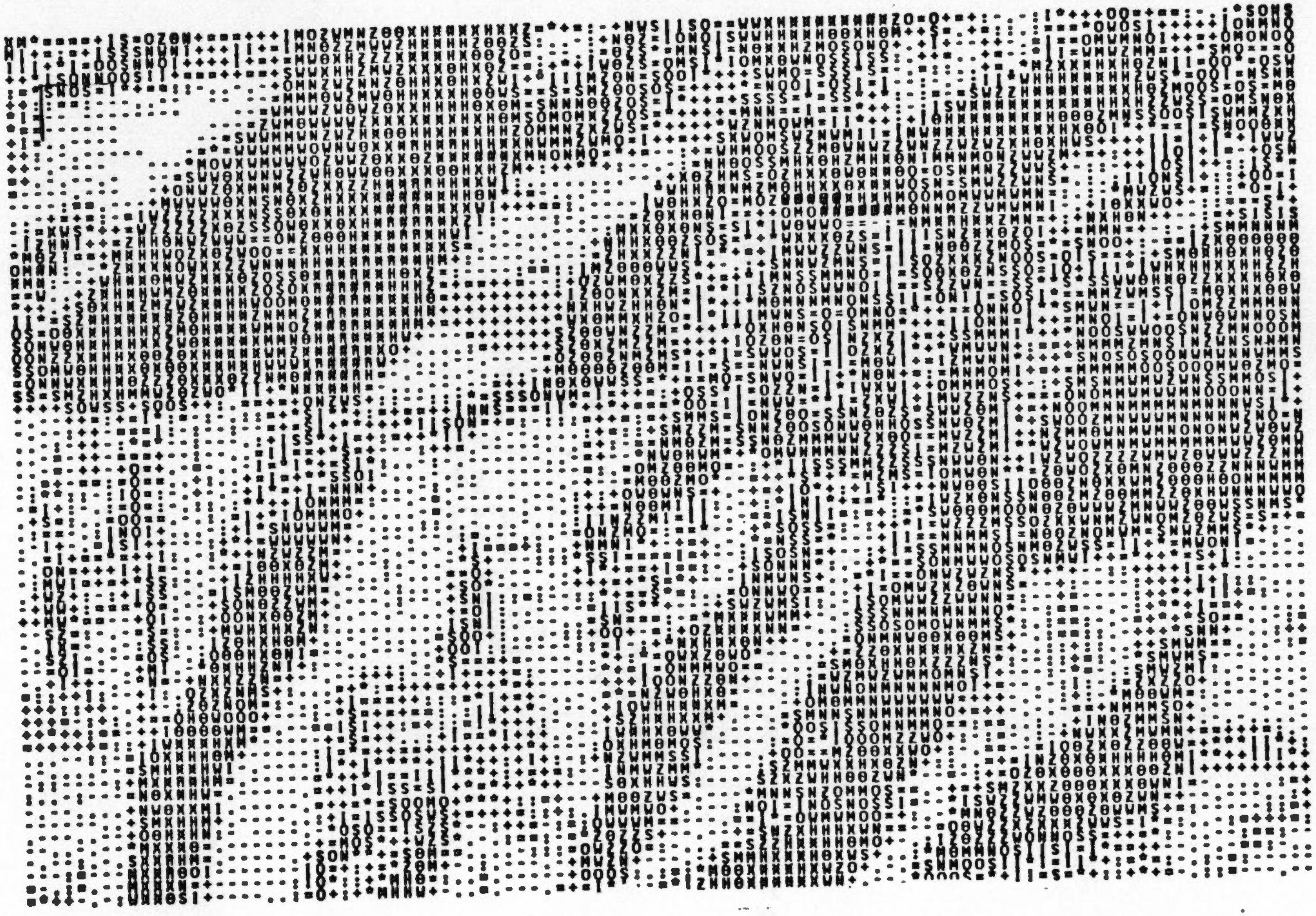

Figure 19. Synthetic image based on the Lambertian model for the Sugartree Gap test site from a DEM centered at (259410E, 3939120N) UTM coordinate.

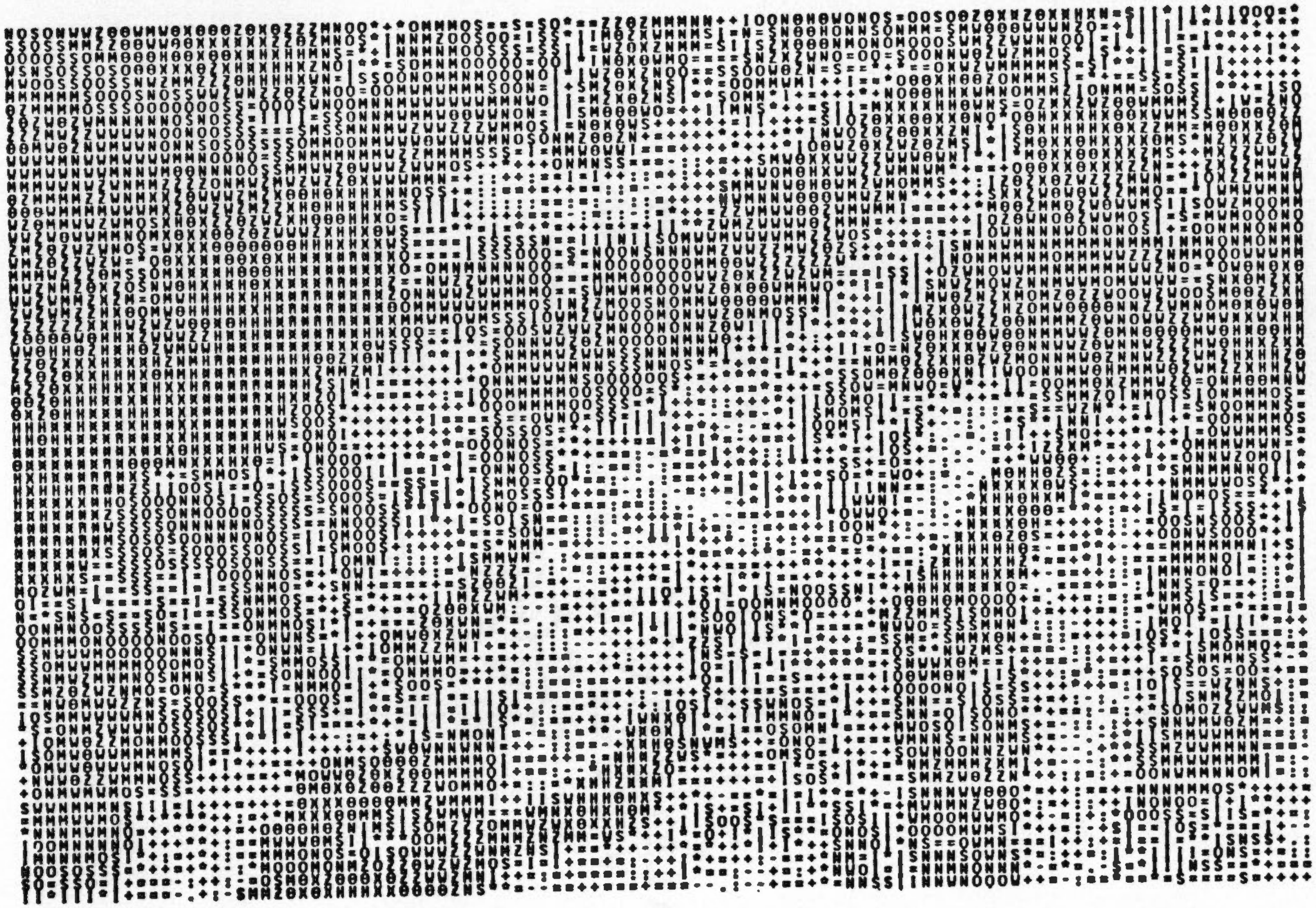

Figure 20. Gray tone image of LANDSAT TM band 4 reflectance for the Rocky Top test site.

Figure 21. Synthetic image based on the Lambertian model for the Rocky Top test site centered at (255410E, 3939120N) UTM coordinate.

Through the visual comparisons and correlation analysis for all seven TM bands, the topographic effects are most noticeable in the spectral range of TM band 4 as expected from the literature for MSS data. This is due to the highest reflected radiance from rugged terrain covered with vegetation being observed in the near infrared (or reflective infrared) and the atmospheric effect being minimized in this particular bandwidth. Also, TM band 5 appeared to have more topographic effect than TM band 4 (Figure 22). This may be due to moisture levels in the canopy vegetation or the onset of leaf fall in some forest cover types. However, no data are available to test either of these suppositions.

TM band 6 shows little, if any, influence of the surface terrain relief under the illumination conditions (Figure 23). However, it might not be useful in vegetation classification anyway since it is the thermal infrared band; also, it has different ground resolution from other bands.

5.1.2 Shadow Representations and the Effects of Solar Incidence Angle

With a reflectance image derived from the Lambertian model, one kind of shadowed region can be readily determined by the local method already described. When a particular surface element has $\cos(i) < 0.0$, that surface element must face away from the sun

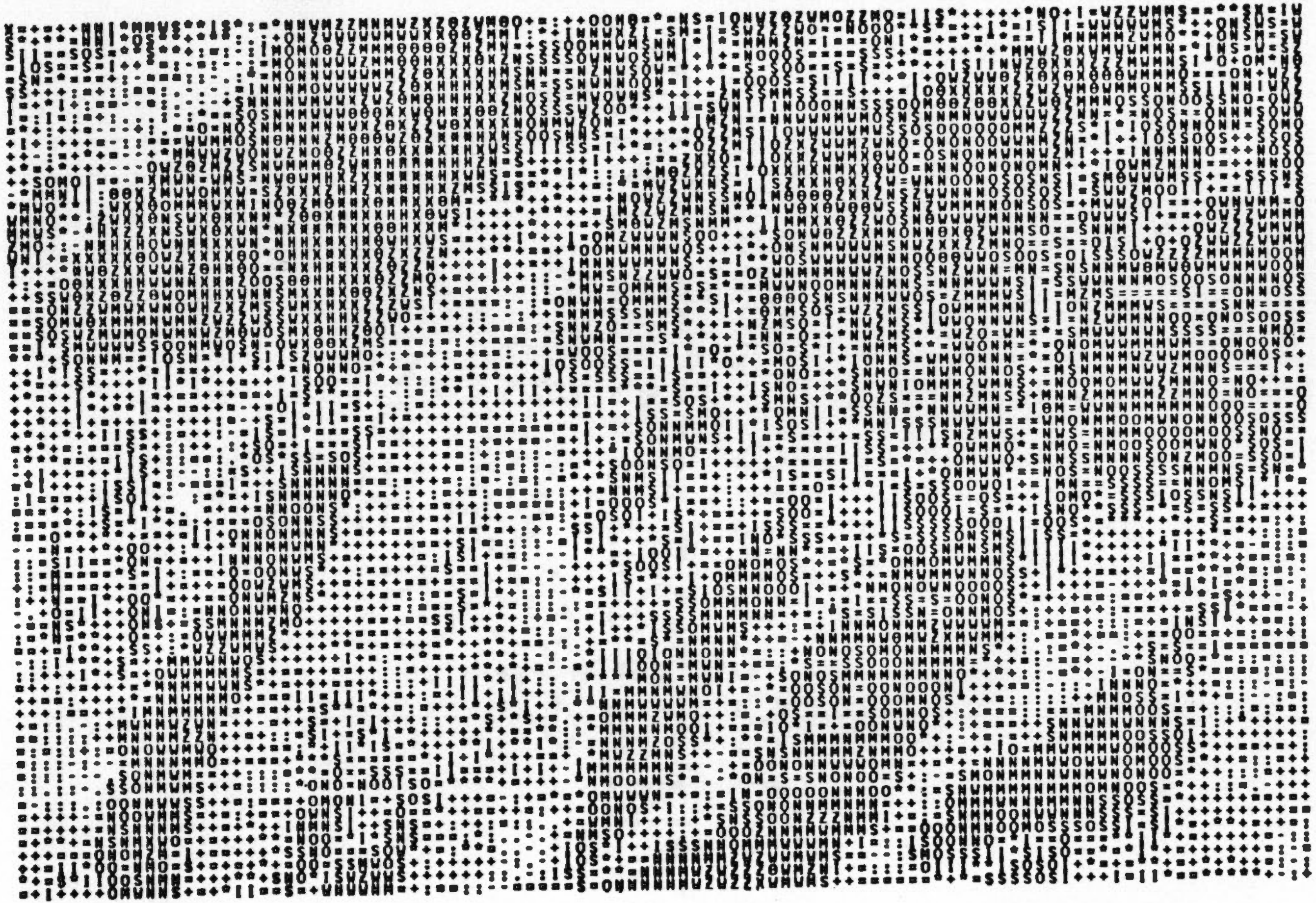

Figure 22. Gray tone image of LANDSAT TM band 5 reflectance of the Sugartree Gap test site.

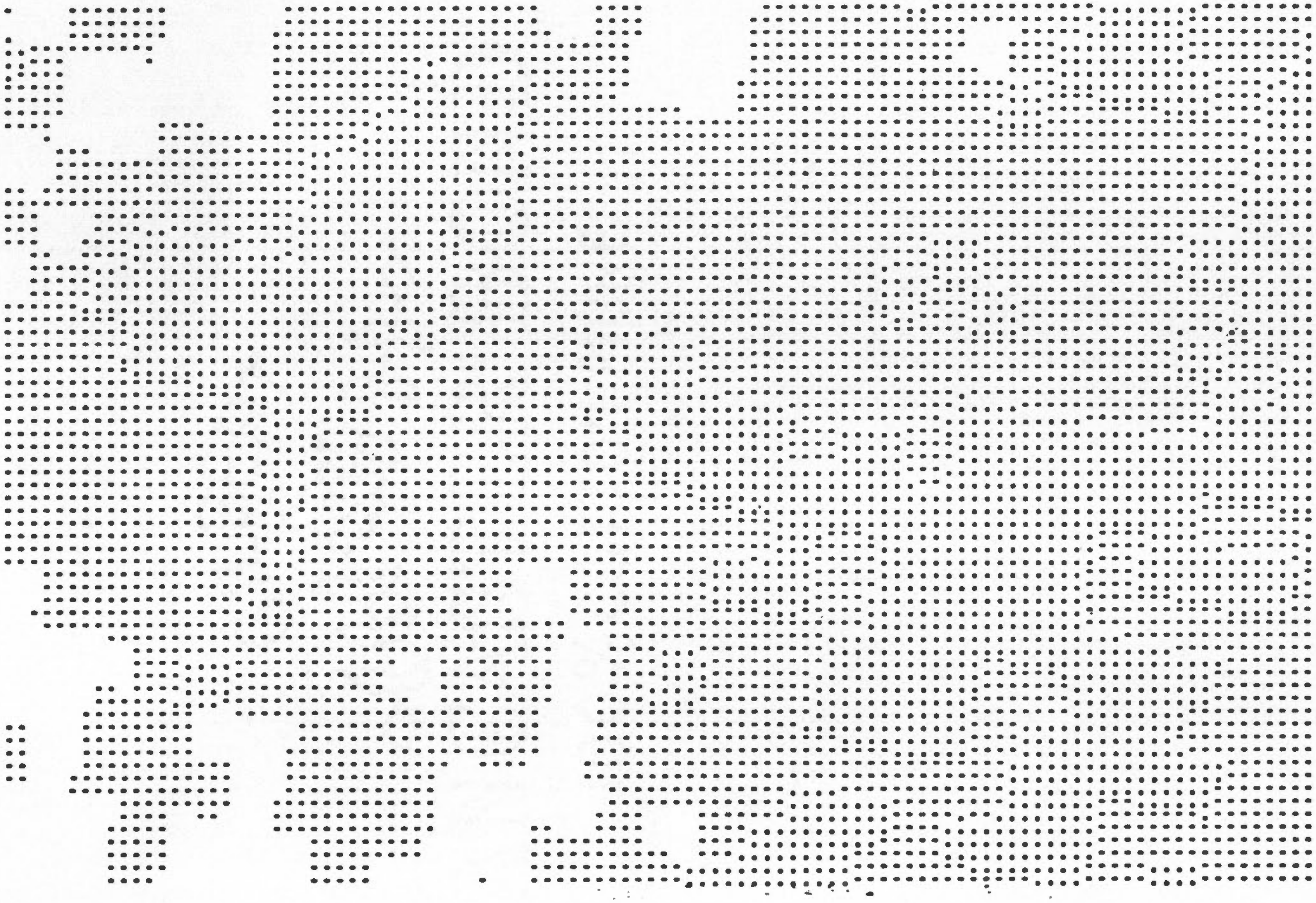

Figure 23. Gray tone image of LANDSAT TM band 6 reflectance of the Sugartree Gap test site.

(i.e., $i > \frac{\pi}{2}$) and is considered as self-shadowed. Figure 24 is a segmented synthetic image created from Lambertian model with a threshold of $i = 71.5^{o}$. The black regions represent the surface elements with incident solar angle (i) equal to or larger than this value. With synthetic image segmented by the threshold of $i = 90^{o}$, self-shadowing can be illustrated explicitly. However, such shadow regions were not found in either test sites.

Other surface elements, however, might face the sun but not receive direct sun illumination because they are obscured by neighboring ridges (i.e., they lie in the shadow cast by other terrain features). Such cast-shadowed region cannot be determined locally; hidden-surface algorithms are needed to predict which surface elements are not visible from the source (Horn and Bachman, 1978). Because the algorithms are quite complex in computation and test areas do not appear to be subject to the effect of cast-shadow based on the visual examination of 3-dimensional perspective maps for both test sites, they are not considered in this study.

In fact, both the self-shadowed and cast-shadowed regions usually occur as small scattered parts within remotely sensed images and their boundaries can be recognized with edge detection techniques.

Besides the self-shadowed regions, the synthetic image can also show the irradiance variations due to topography, with various tones of shading corresponding to different incident angles (i.e., $90^{o} > i > 0^{o}$). The continuous changes of brightness values caused by the orienta-

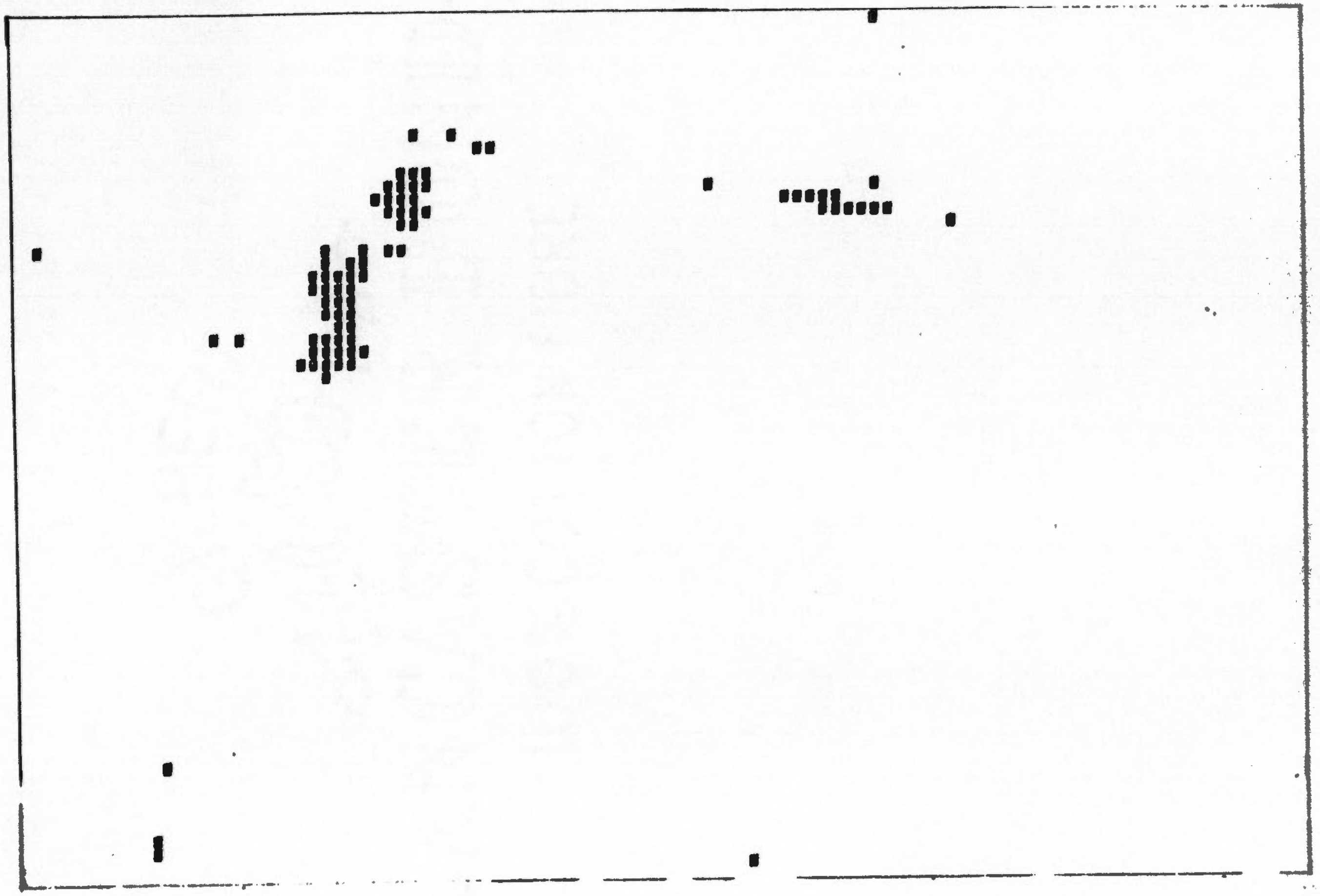

Figure 24. The binary image segmented by a threshold of the solar incidence angle i = 71.5° for the Sugartree Gap test site.

tion, a synthetic image was segmented with a cut-off point of $i = 55^{\circ}$. Thus, the surface elements with incidence solar angle equal to or larger than this threshold were assigned to zero intensity value; otherwise, 31 was assigned (Figure 25). Comparing it with Figure 10 and 22, we can clearly see that the areas of low reflection brightness values in TM4 and TM5 basically correspond to those areas with effective incidence angles larger than about 55°; this is due to the local topographic features rather than the intrinsic scene properties.

Since cover types tend to vary with elevation, slope and aspect regimes, the brightness values obtained from remote sensing are combinations of their irradiance and vary with geography and location. The separation of topography and surface cover types in terms of remote sensing digital imagery is a difficult task. So far, many investigations have been focused on the relationship between various vegetation types and different terrain features (slopes, aspects, and elevations), but satisfactory elimination of the continuous variations due to topography has not yet been demonstrated.

To utilize the information provided by a synthetic image simulating topographic variations, the synthetic brightness has to be converted into discrete data and combined with a real LANDSAT image. This will require that the multiple thresholds be selected carefully so as to segment shading regions in a LANDSAT image.

Figure 25. The binary image of the Sugartree Gap area generated by segmenting a synthetic image with the solar incidence angle i =55°

5.1.3 Evaluation on the Two Reflectance Models

Synthetic image of the Sugartree Gap test area was generated by the Lommel-Seeliger model (Figures 26). When compared with that based on the Lambertian model (Figure 19), no large differences are evident, except that the contrast of various shading of the latter is not as impressive as that of the former. This difference can be explained by the Lommel-Seeliger model taking the viewing angle effect into consideration in a specific way and modifying the effect of incidence illumination angle by decreasing the saturation level of simulating radiance value.

This difference can be better demonstrated by comparing the scatter plots of synthetic images from the two different models with the LANDSAT TM band 4 image (Figures 15 and 27). Even though with the same scaler (i.e., u = 255), the synthetic brightness values from the Lambertian model (Figure 15) are much higher than those from the Lommel-Seeliger model (Figure 27). In addition, the range of synthetic brightness values from the Lommel-Seeliger model is basically corresponding to the range of the TM4 reflectance, thus the scattering plots in Figure 27 are closer about the predicted straight line than that in Figure 15. As a result, the Lommel-Seeliger model was used to carry out correlation and linear regression analysis with the real TM image, even though the correlation coefficient is not much higher than that of the Lambertian model (Table 3).

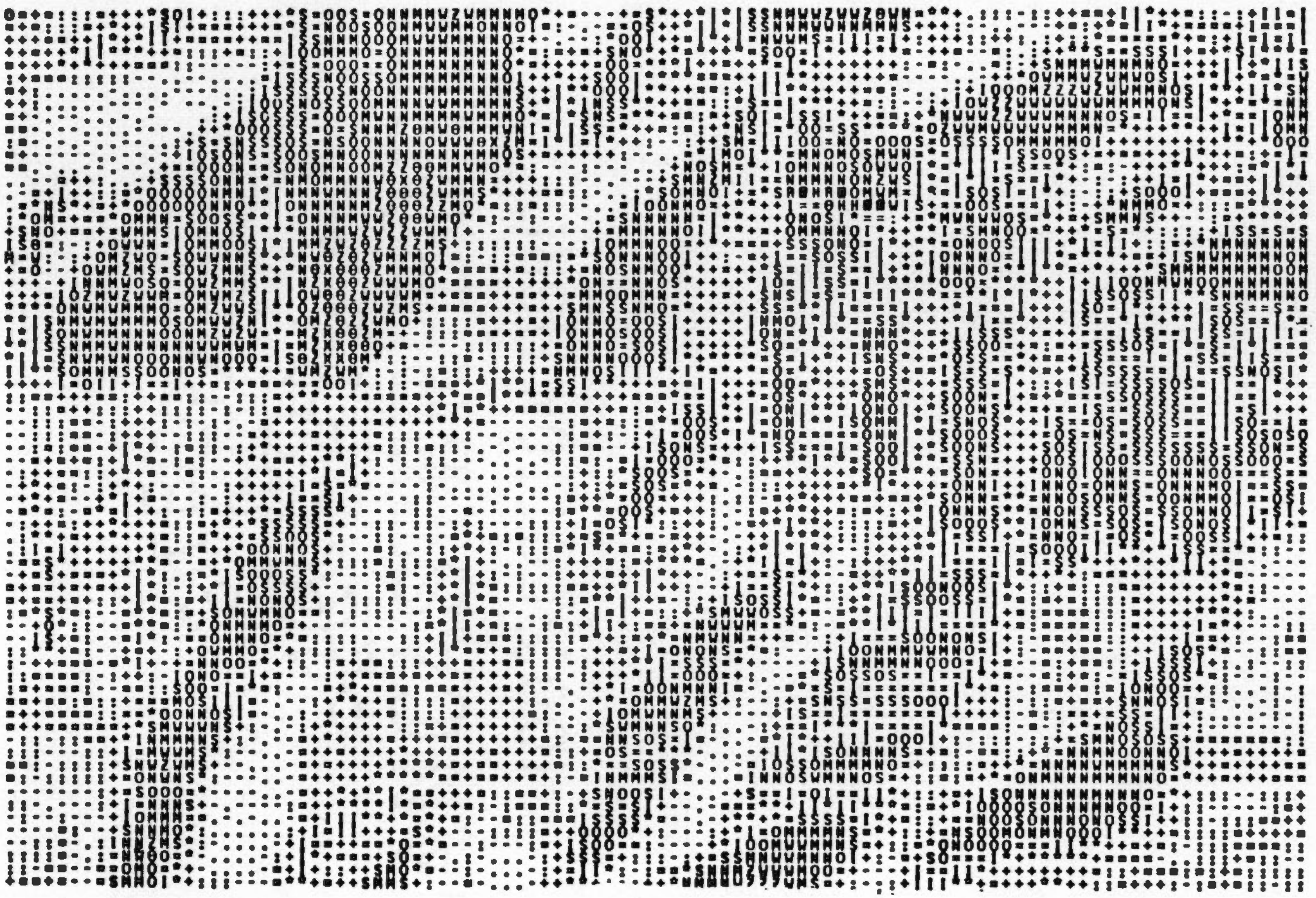

Figure 26. Synthetic image of the Sugartree Gap test site based on the Lommel-Seeliger model.

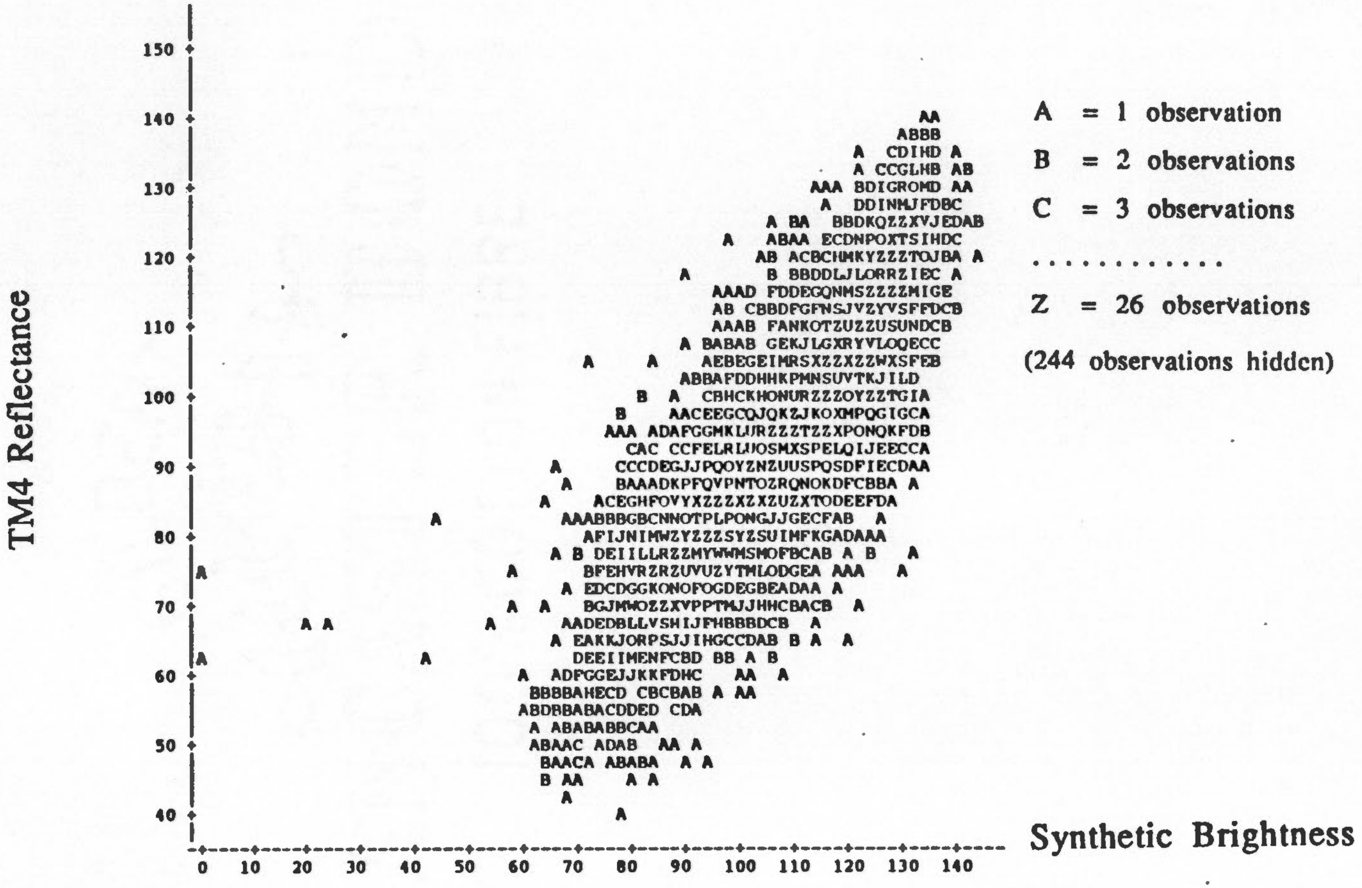

Figure 27. A scatter plot of TM band 4 refectance versus the synthetic brightness of the Lommel-Seeliger model for Sugartree Gap test site (7038 pixels).

5.1.4 Correlation of Synthetic Images and TM Data

Statistically significant correlations are found between LANDSAT TM data and effective incidence angle of solar illumination, which varies with different spectral TM bands. Tables 3 and 4 show the values of correlation coefficient (R) of each TM band and synthetic images generated from both the Lambertian and the Lommel-Seeliger models for the Sugartree Gap and the Rocky Top test site, respectively. The highest correlation coefficients are from 0.825 to 0.854 in TM4 and TM5; they vary slightly with different test sites. These results indicate that these two variables (the cosine of incident solar angle and TM4 or TM5) have a very close linear relationship; about 69% to 73% of variation of TM4 or TM5 reflectance can be explained by the effect of the cosine of solar incidence angle.

The correlations are stronger in TM bands 4 and 5 than they are in other bands. The smaller effect at either shorter or longer wavelength is likely due to greater atmospheric scattering and weaker reflectance from vegetation.

Table 3. Correlation coefficients of LANDSAT TM spectral bands and synthetic brightness from two reflectance models (Sugartree Gap Test site)

Bands	Lambertian model R	Lommel-Seeliger model R
1	0.636	0.637
2	0.752	0.751
3	0.714	0.710
4	0.825	0.832
5	0.854	0.854
6	0.450	0.472
7	0.730	0.731

* R is the correlation coefficient.

Table 4. Correlation coefficients of LANDSAT TM spectral bands and synthetic brightness from two reflectance models (Rocky Top test site)

Bands	Lambertian model R	Lommel-Seeliger model R
1	0.685	0.683
2	0.772	0.757
3	0.727	0.706
4	0.832	0.837
5	0.845	0.826
6	0.572	0.609
7	0.738	0.710

5.2 Registration of the LANDSAT TM Image and the DEM Data

As shown in section 4.2, good registration between LANDSAT TM images and DEM data can be achieved by corresponding patterns of the synthetic brightness and TM reflectance. The approach has been successful in overall registration of LANDSAT TM image with DEM data in the two test sites of this study. However, exact point to point correspondence still cannot be assured, because (1) there is still some effect of various cover types in the TM image; (2) there is slight variations in the LANDSAT spectral reflectance from TM4 to TM5; and (3) the synthetic brightness models may have some errors.

On the other hand, the surface model registered to the LANDSAT TM image will inherit the geometric errors existing in TM images since these images were used as a reference rather than a standard map. Obviously, geometric rectification of DEM data to the ground can be achieved only through the use of ground control points.

5.3 Evaluations of Scatter Plots and Residual Images

5.3.1 The Relations between LANDSAT TM Bands and Synthetic Image

A measure of the relation between TM images and synthetic images can be obtained by plotting TM reflectance versus synthetic brightness for all points in the matched images. Figures 27 to 33 show these plots for the Sugartree Gap test site. All of these scatter plots are created by plotting each TM band reflectance against the synthetic brightness from the Lommel-Seeliger model. As discussed in the development of equation (30), residuals from the linear model of TM and synthetic images depend on the parameters a and b, as well as the difference between real reflectance factor u(x,y) and fixed value of u. Each TM spectral band has different capabilities of transmitting through the atmosphere and selected receiving of the radiance reflected or emitted from ground materials. Thus, the differences among these scatter plots can be accounted for by the variations of atmosphere and the component of ground features received at different wavelength. Therefore, it should be possible to estimate the parameters of atmospheric effect with the slope and intercept, and to demonstrate the different sensing function of each TM spectral band with the disparity of scattering plots for a homogeneous ground cover type.

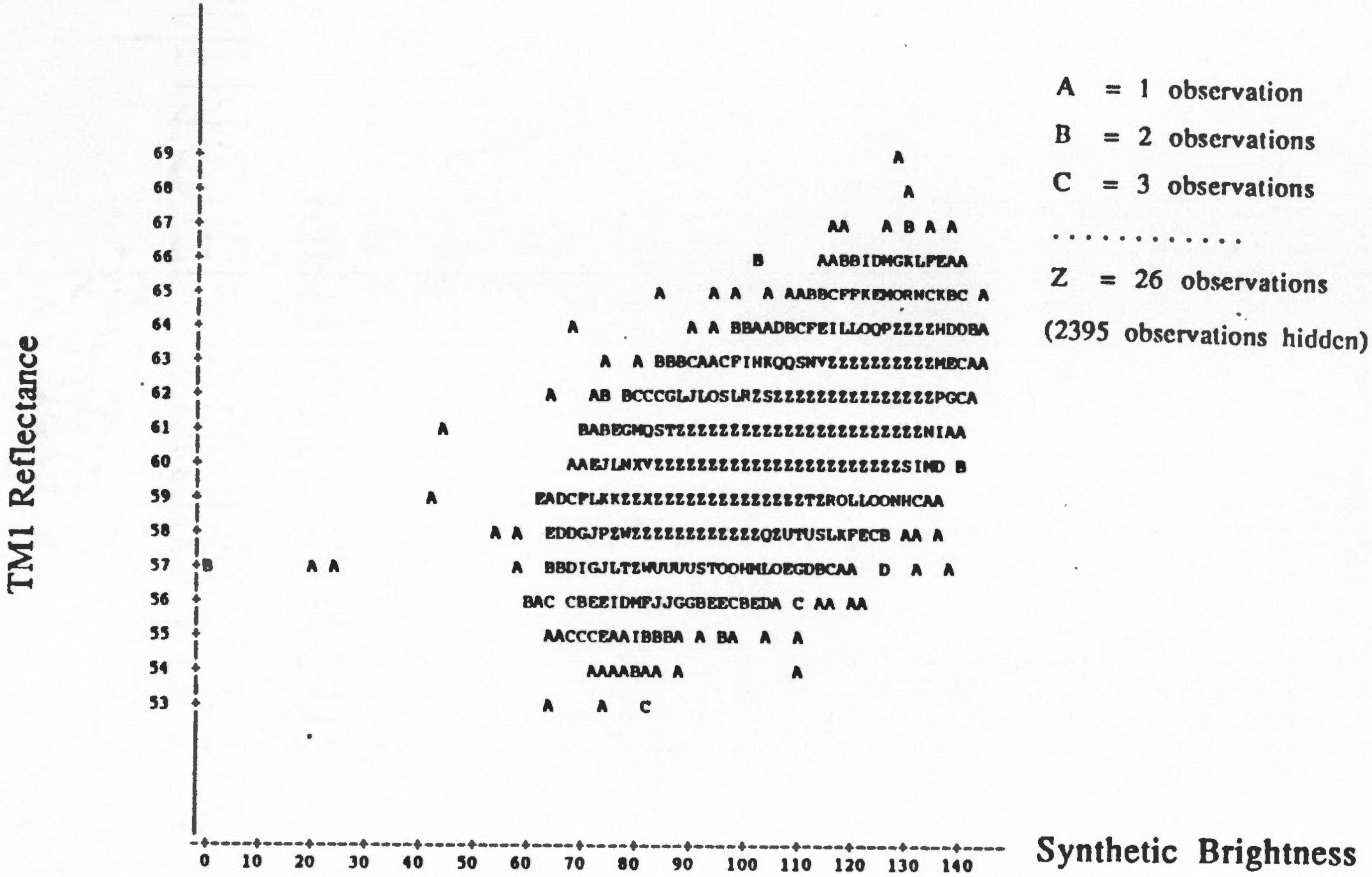

Figure 28. A scatter plot of TM band 1 reflectance versus the synthetic brightness of the Lommel-Seeliger model for the Sugartree Gap test site (7038 pixels).

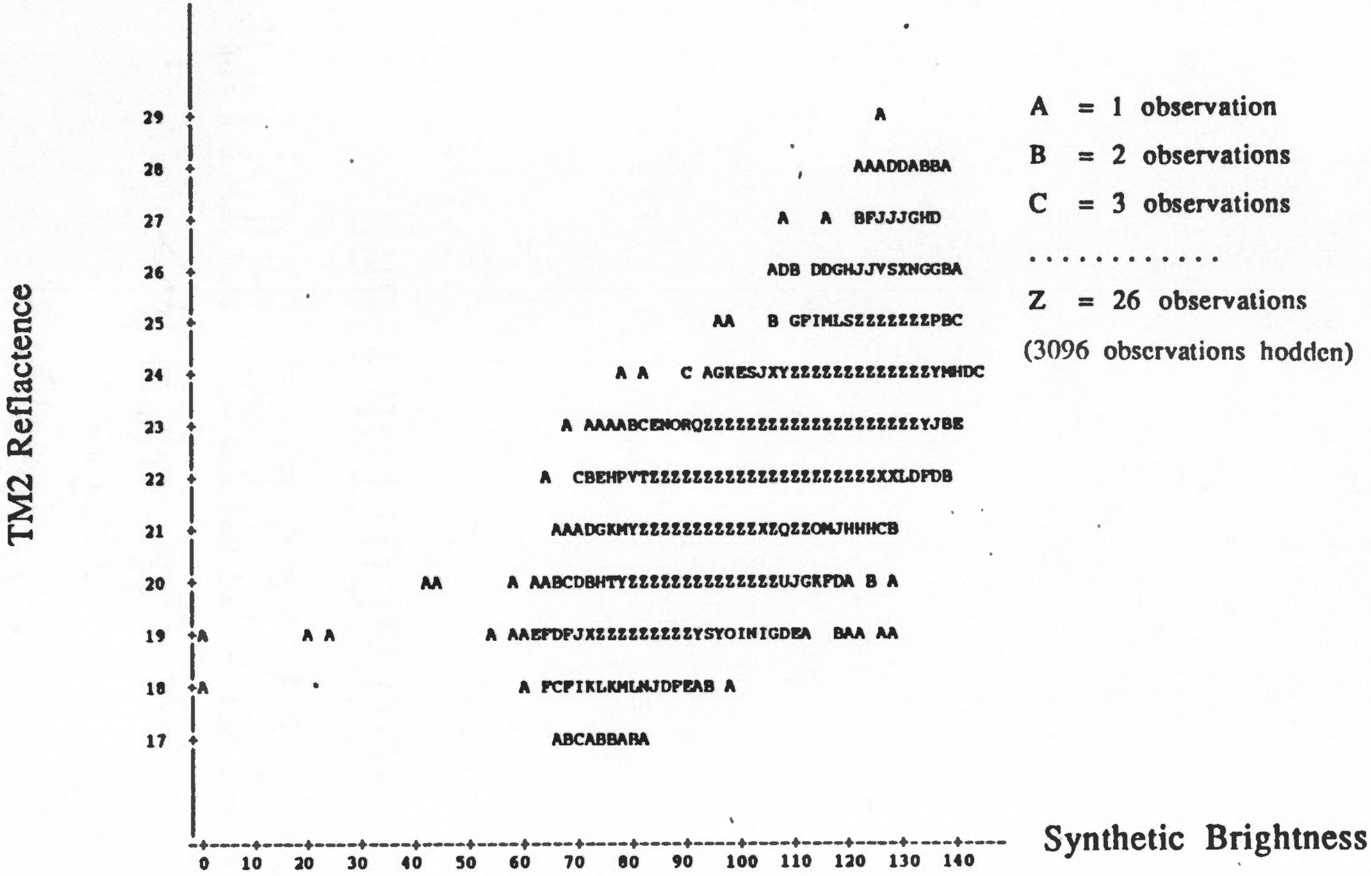

Figure 29. A scatter plot of TM band 2 reflectance versus the synthetic brightness of the Lommel-Seeliger model for the Sugartree Gap test site (7038 pixels).

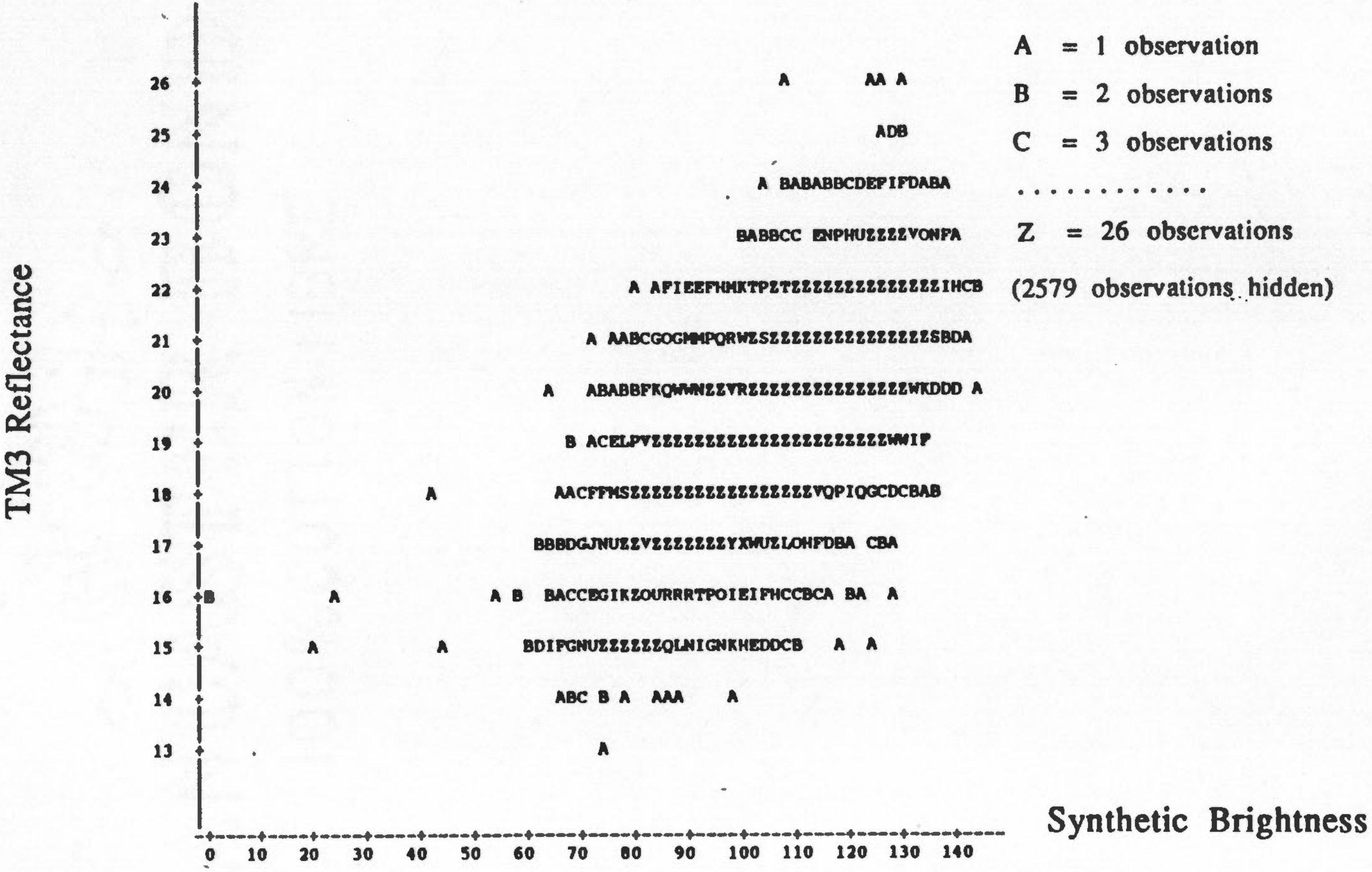

Figure 30. A scatter plot of TM band 3 reflectance versus the synthetic brightness of the Lommel-Seeliger model for the Sugartree Gap test site (7038 pixels).

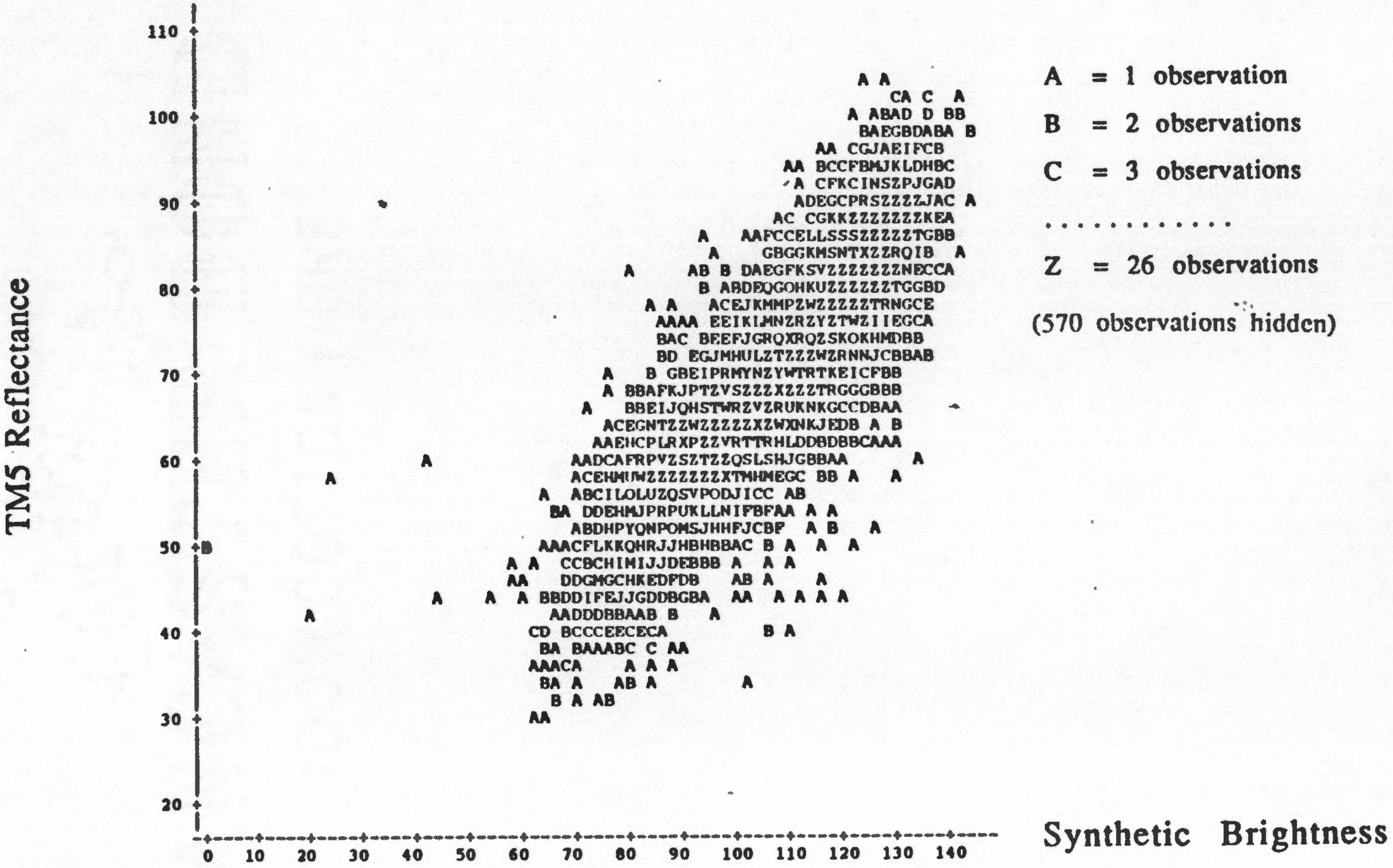

Figure 31. A scatter plot of TM band 5 reflectance versus the synthetic brightness of the Lommel-Seeliger model for the Sugartree Gap test site (7038 pixels).

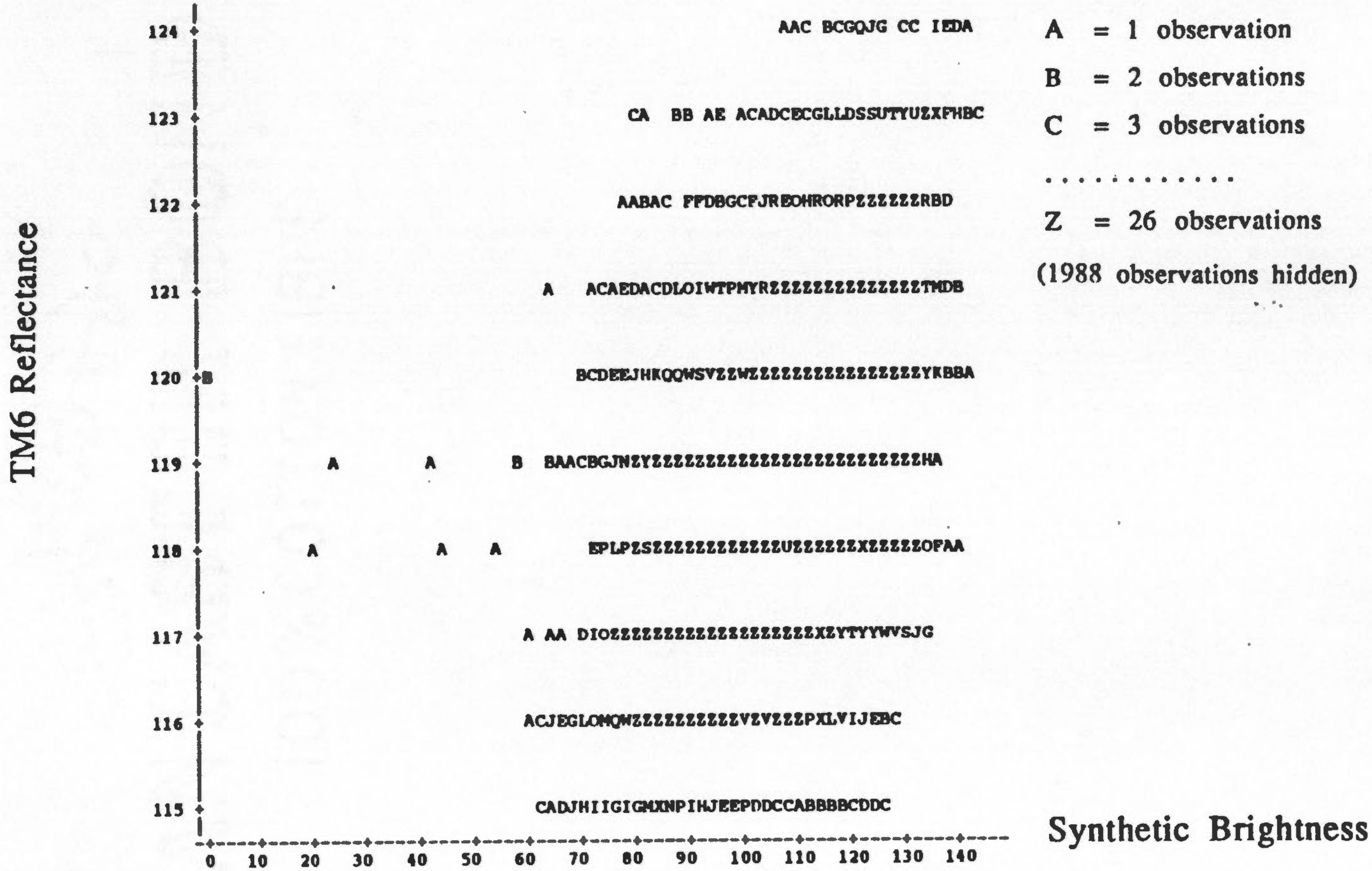

Figure 32. A scatter plot of TM band 6 reflectance versus the synthetic brightness of the Lommel-Seeliger model for the Sugartree Gap test site (7038 pixels).

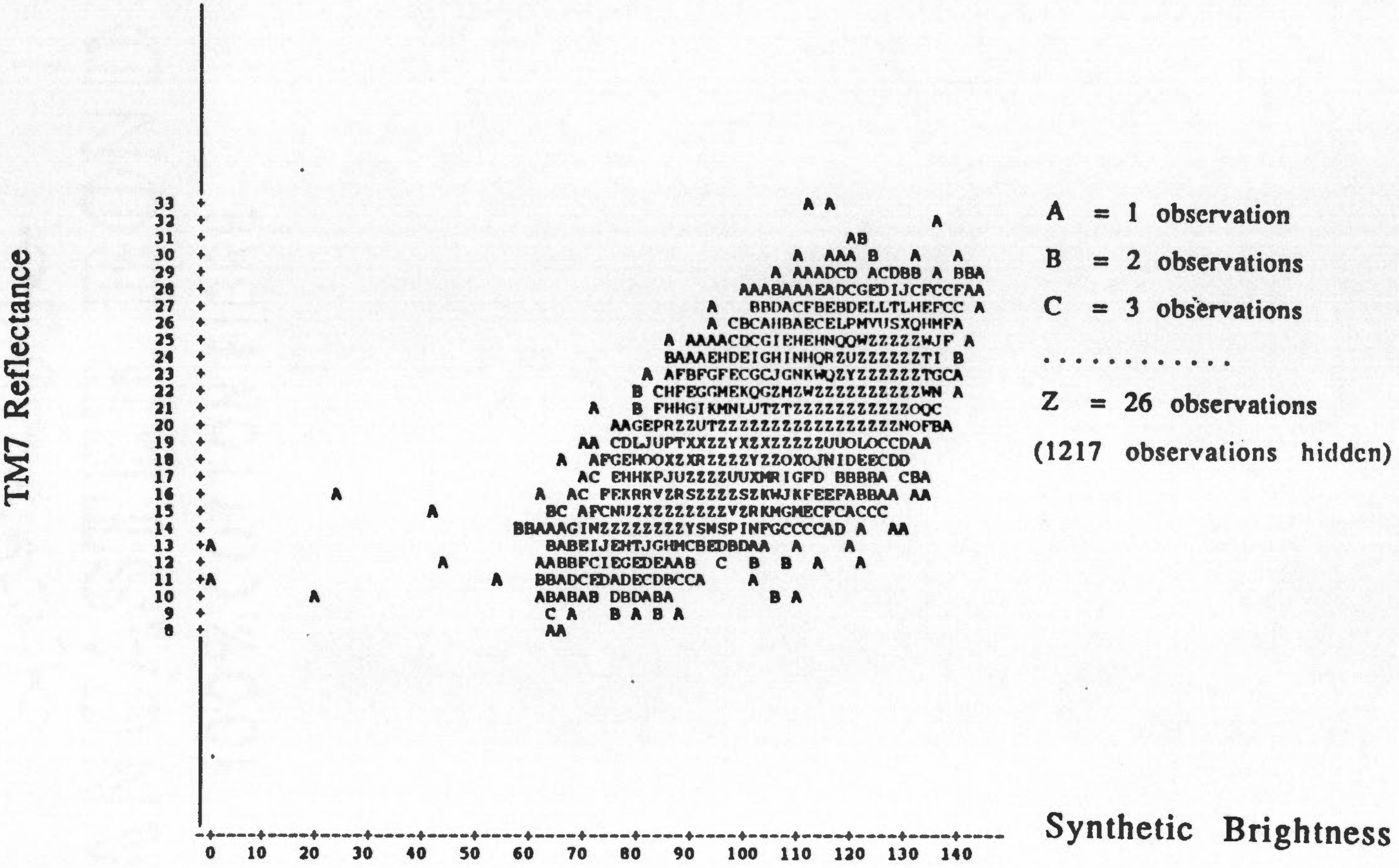

Figure 33. A scatter plot of TM band 7 reflectance versus the synthetic brightness of the Lommel-Seeliger model for the Sugartree Gap test site (7038 pixels).

On the other hand, in a specific TM spectral band, the parameters a and b are assumed to be the same; then the difference of $T(x, y) - \hat{T}(x', y')$ could be explained as the local deviation of $u(x, y)$ from the assigned value for u, which is related to the different reflecting cover types. Thus, the residuals from the straight line implicated in linear regression model represent various ground patterns with homogeneous spectral intensities. Since TM4 and TM5 are primarily responsive to vegetation types and behave basically as Lambertian reflector in these two test sites (as stated in previous sections), the gray tone images of the residuals from both TM4 and TM5 versus the Lambertian synthetic brightness were created and shown in next section.

5.3.2 Original and Segmented Residual Images

Figures 34 and 35 are the residual images from TM4 and TM5 versus the Lambertian synthetic brightness for the Sugartree Gap test site.

Figures 36 and 37 are the segmented residual images using equation (31), emphasizing the middle range of gray levels. While Figures 38 and 39 are those using equation (32) which better discriminates at the extremes of gray levels. By the comparisons of these images, the features in middle range of the scaled residuals (corresponding to the range around the value of zero of the original

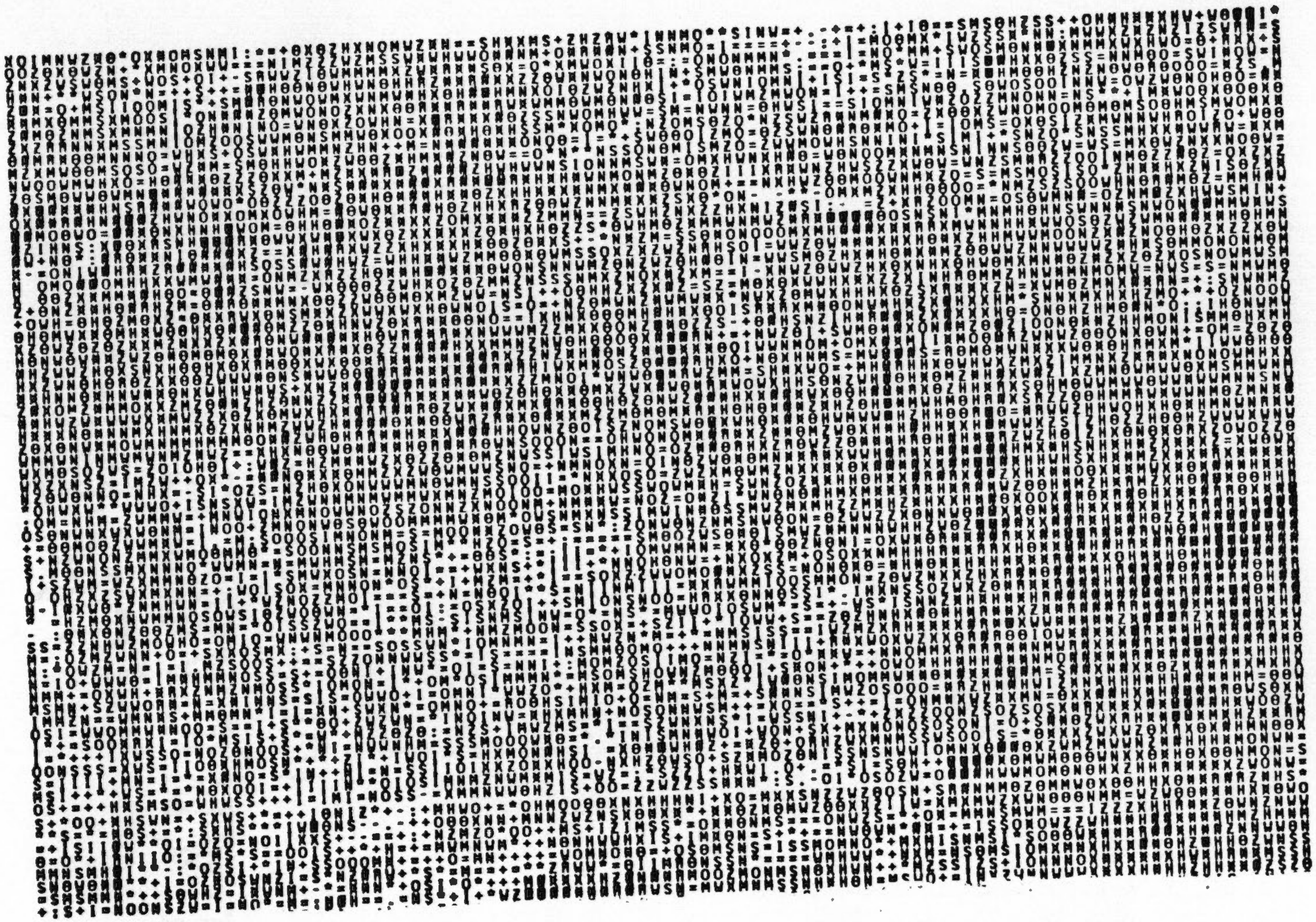

Figure 34. A residual image from the linear regression of TM4 reflectance and the Lambertian synthetic brightness for the Sugartree Gap test site.

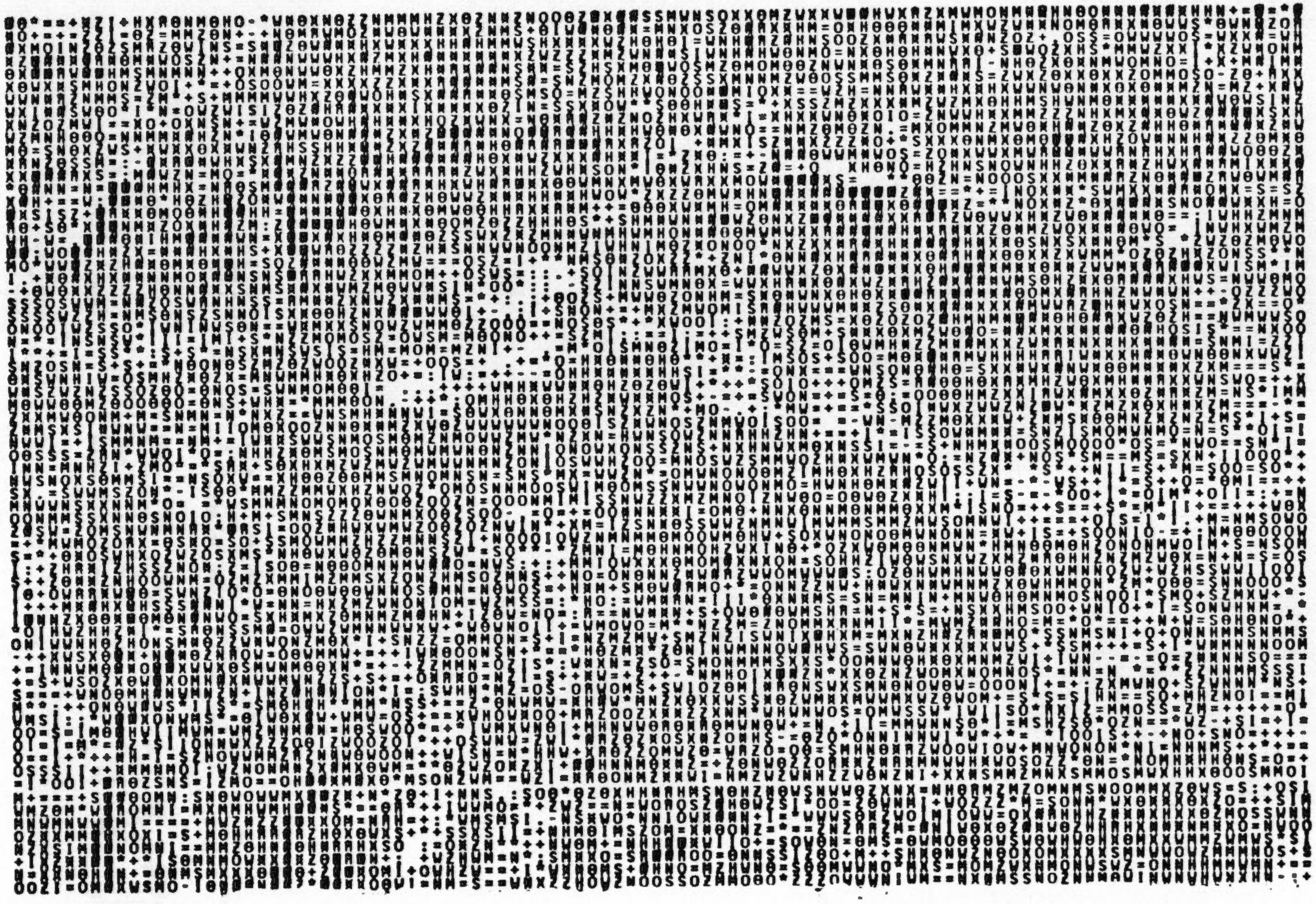

Figure 35. A residual image from the linear regression of TM5 reflectance and the Lambertian synthetic brightness for the Sugartree Gap test site.

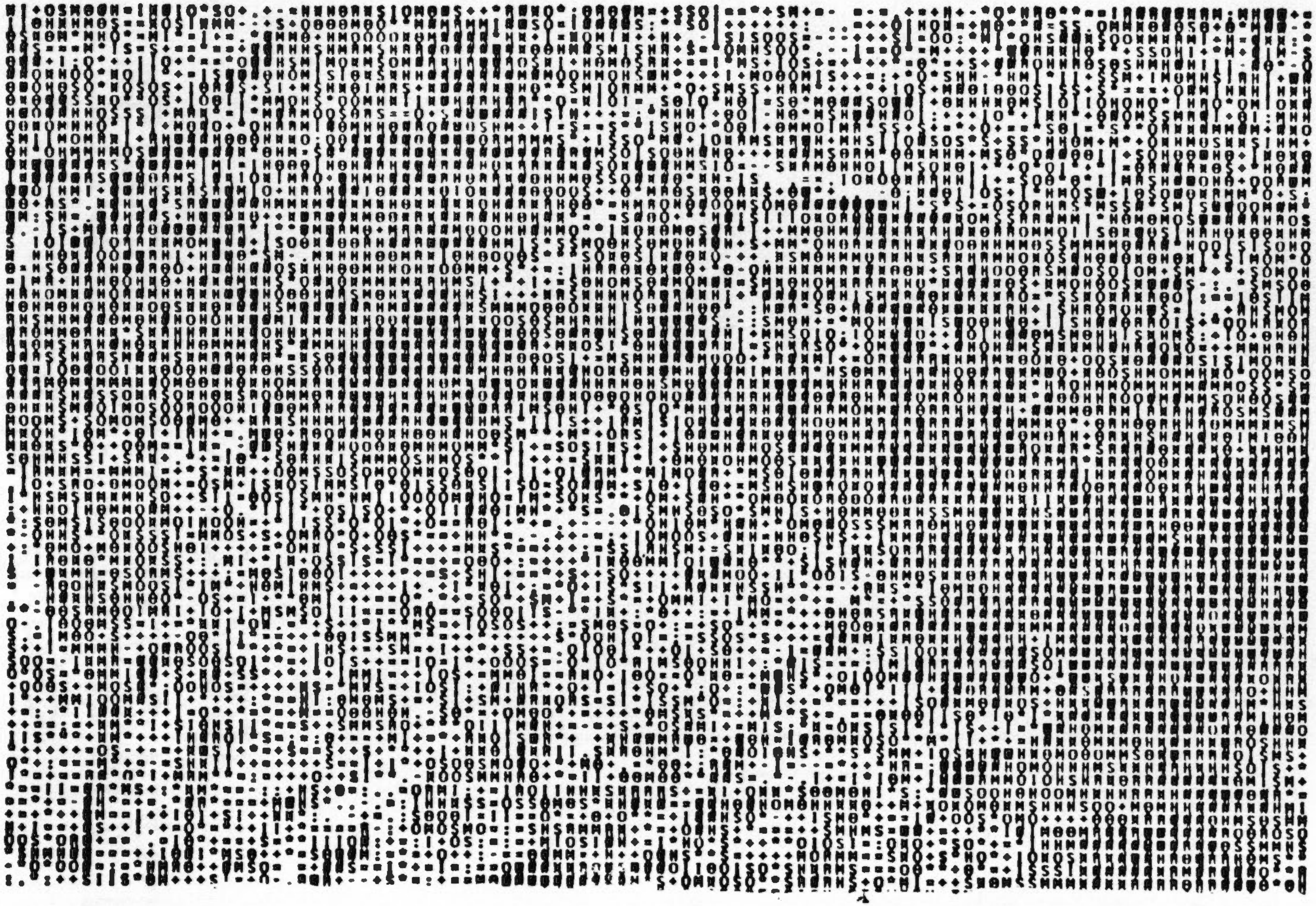

Figure 36. A residual image from TM4 and the Lambertian model segmented by Equation (32) for the Sugartree Gp test site.

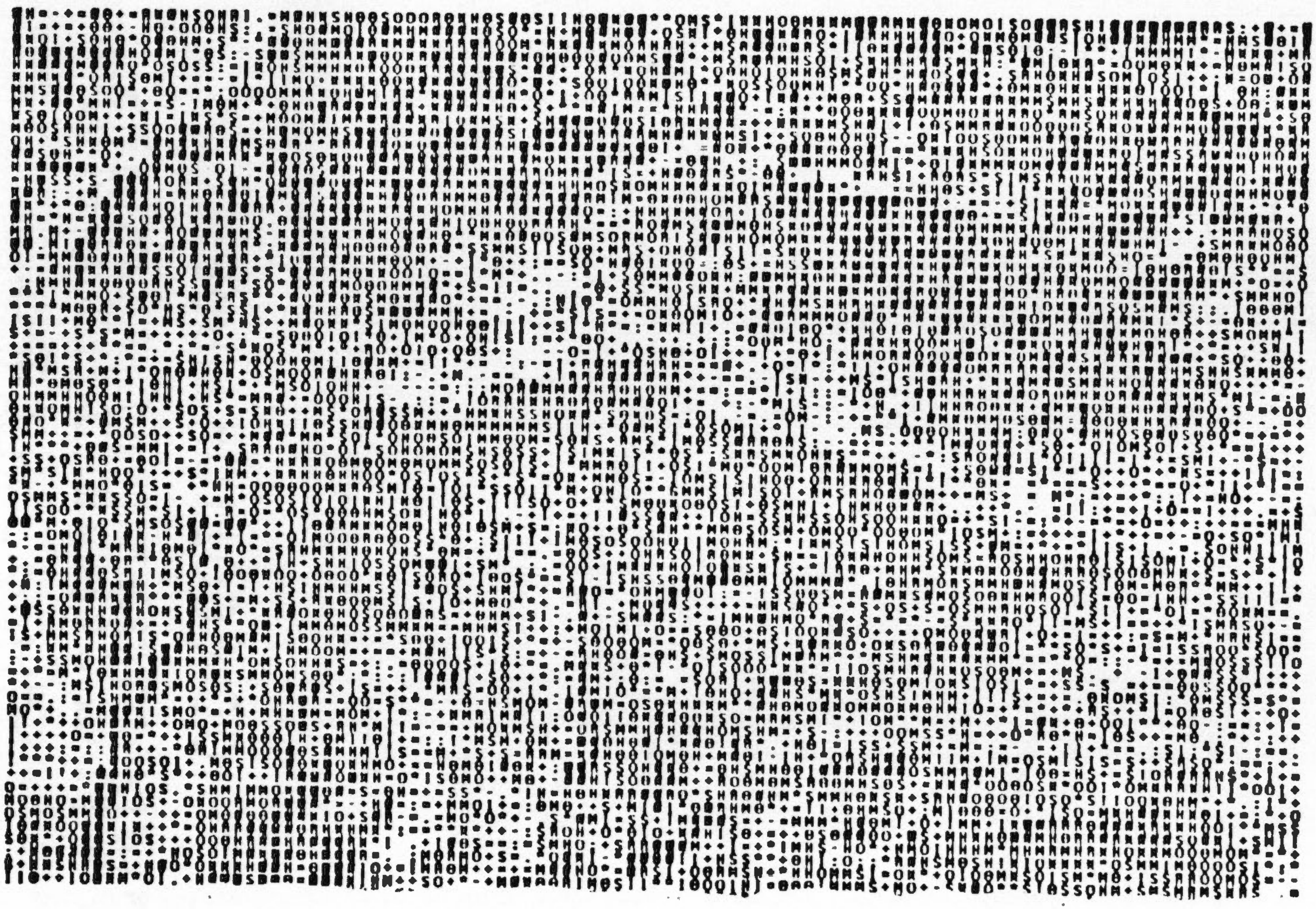

Figure 37. A residual image from TM5 and the Lambertian model segmented by Equation (32) for the Sugartree Gap test site.

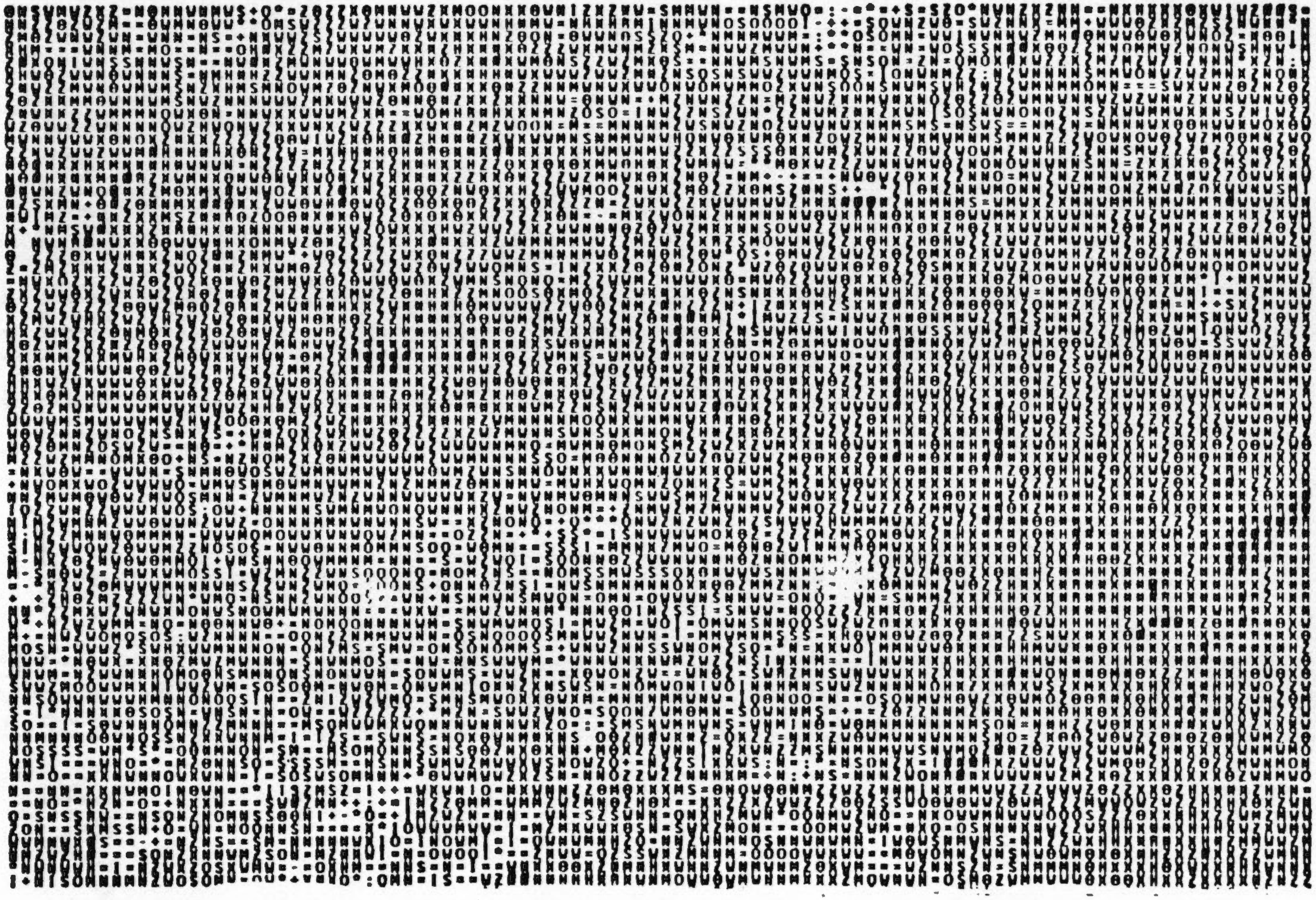

Figure 38. A residual image from TM4 and the Lambertian model segmented by Equation (33) for the Sugartree Gap test site.

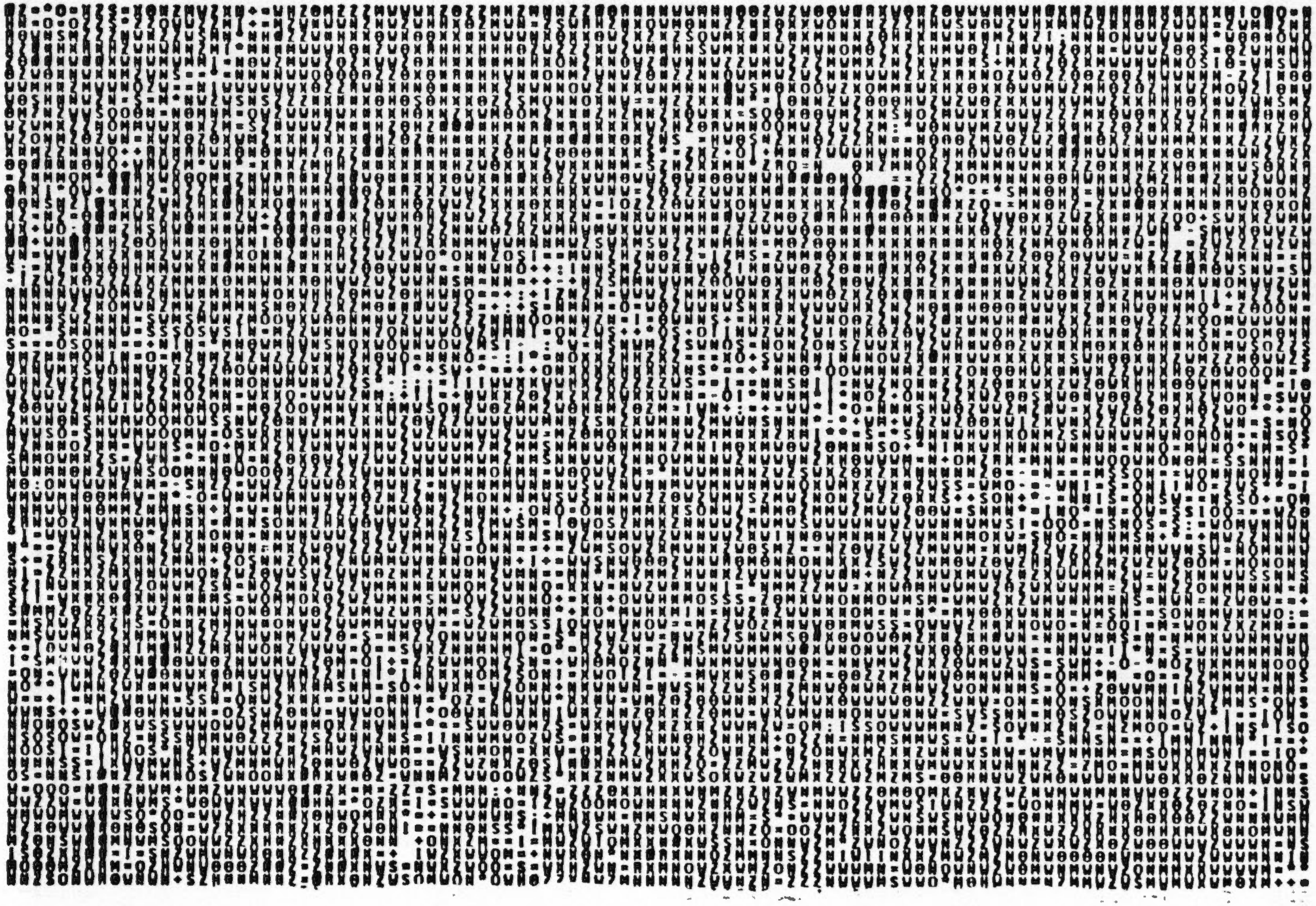

Figure 39. A residual image from TM5 and the Lambertian model segmented by Equation (33) for the Sugartree Gap test sie.

residuals) were better expressed in Figures 36 and 37; (this conclusion is based on the observation at the boundaries of shading regions). In contrast, Figures 38 and 39 clearly demonstrate the features with the large residuals from linear model of TM reflectance and synthetic brightness. The blurring appearance of these two images might be due to the limitations of 32-levels gray tone display, but, it may be also due to the homogeneous spectral features of deciduous vegetation.

If a field-based cover type map were available, more sophisticated extracting techniques could be utilized to classify ground spectral patterns more precisely. These include segmentation based on multi-dimensional histograms and cluster analysis,

5.4 Limitations of The Study

The following limitations must be recognized:

** Only one LANDSAT TM image was utilized for the study.

** No high resolution digital displaying equipment was available for this study.

** Mutual illumination of surface elements and atmospheric effects were not taken into account.

** No cover type map based on ground examination was available as a reference.

** Local errors were present in the sample DEM data used.

5.5 Conclusions

The following conclusions can be made from this study.

** The reflectivity of the original LANDSAT TM data was influenced more by local topographic features rather than the reflectance properties of ground materials in these mountainous study areas, especially in the regions with solar incidence angle larger than 55°.

** Synthetic images can be utilized effectively to register remotely sensed data to digital terrain model. They provide a practical and useful way to match these two data sets of different nature, especially in rugged terrain regions where no apparent ground features can be found as reference points or in unassesable areas.

- ** Statistically significant correlation coefficients were found between LANDSAT thematic mapper data and the cosine of incident angle of solar illumination in both test sites. They vary slightly with different topographic environments and different deciduous vegetation types.

5.6 Recommendation for Further Research

Based on this study, the following areas should be considered for further investigation.

- ** The relief displacement effects in both TM and DEM data should be investigated if a highly accurate classification is obtained.

- ** The adoption of non-Lambertian reflectance models should be tested in different mountainous regions having different vegetation types.

- ** The shaded-relief synthetic imagery should be utilized in Geographic Information System (GIS) as the surface gradient layer for overlaying analysis.

** Since residual data generated from most TM bands tend to have a Gaussian distribution with the mean of zero, they might be used to execute classifying ground cover patterns by the maximum likehood classification algorithm.

** Cluster analysis of residual data can be attempted to get an insight into ground cover spectral patterns, hopefully, with the elimination of most or all of the topographic effect. However, the test should include all of the different combinations of variables, such as the residual data from different TM bands, residual images and elevation data, and even residual data with TM data.

** Quantitative evaluation of the effect of DEM quality on topographic simulations and corrections should be investigated.

BIBLIOGRAPHY

Bibliography

Batson, R.M., K. Edwards and E.M. Eliason. 1975. Computer-generated shaded-relief images. *J. Res. U.S. Geol. Survey* **3**:401-408.

Bhanu, Bir and Bahram a. Parvin. 1987. Segmentation of natural scenes. *Pattern Recognition* **20**:487-496.

Blinn J.F. 1977. Models of light reflection for computer synthesized pictures. *SIGGRAPH-ACM* **11**:192-198.

Carter, J.R. 1987. Evaluation of the 1:250,000 digital elevation model for use in a GIS for the Great Smoky Mountains National Park. *Proceedings of the International GIS Conference. 1987.* (in press).

Dave, J.V. and R. Bernstein. 1982. Effect of terrain orientation and solar position on satellite-level luminance observations. *Remote Sensing of Environment* **12**:331-348.

Egbert, D.D. 1977. A practical method for correcting bidirectional reflectance variations. *Proceedings of Machine processing of Remotely Sensed Data Symposium.* **1977**:178-185.

Fleming, M.D. and R.M. Hoffer. 1979. Machine processing of Landsat MSS data and DMA topographic data for forest cover type mapping. *LARS Technical Report 062879.*

Gonzalez, R.C. and P. Wintz. 1987. Digital Image Processing. Second edition. Addison-Wesley Publishing Company, Inc. 503 pp.

Goodenough, D.G. 1979. The image analysis system (CIAS) at the Canada center for remote sensing. *Canadian Journal of Remote Sensing* **5**:3-17.

Guo, Defang. 1987. Computer Processing and Pattern Recognition of Remotely Sensed Imagery (in Chinese). Electronic Industrial Publisher. 448 pp.

Hall-Konyves, K. and L. Olsson. 1984. Empirical studies of the relationship between Landsat MSS data and topography. *Proceedings of the Eighteenth International Symposium on Remote Sensing of Environment.*

Holben, B.N. and C.O. Justice. 1979. Evaluation and modeling of the topographic effect on the spectral response from nadir pointing sensors. *NASA Technical Memorandum 80305.*

Holben, B.N. and C.O. Justice. 1981. An examination of spectral band ratioing to reduce the topographic effect on remotely sensed data. *Int. J. Remote Sensing* **2**:115-133.

Horn, B.K.P. 1977. Understanding image intensities. *Artificial Intelligence* **8**:201-231.

Horn, B.K.P. and B.L. Bachman. 1978. Using synthetic images to register real images with surface models. *Commun. Ass. Comput. Mach.* **21**:914-924.

Horn, B.K.P. 1981. Hill shading and the reflectance map. *Proceedings of the IEEE* **69**:14-47.

Hugli, H. and W. Frei. 1981. Correcting for anisotropic reflectances in remotely sensed images from mountainous. *Proceedings of Machine Processing of Remotely Sensed Data Symposium.* **1981:363-374.**

Hugli, H. and W. Frei. 1983. Understanding anisotropic reflectance in mountainous terrain. *Photogrammetric Engineering and Remote Sensing* **49**:671-683.

Hutchinson, H.C. 1982. Techniques for combining Landsat and ancillary data for digital classification improvement. *Photogrammetric Engineering and Remote Sensing* **48**:123-130.

Jensen, J.R. 1986. Introductory Digital Image Processing: A Remote Sensing Perspective. New Jersey: Prentice-Hall.

Justice, C.O. and B.N. Holben. 1979. Examination of Lambertian and non-Lambertian models for simulating the topographic effect on remotely sensed data. *NASA Technical Memorandum 80557.*

Justice, C.O., S.W. Wharton and B.N. Holben. 1981. Application of digital terrain data to quantify and reduce the topographic effect on Landsat data. *Int. J. Remote Sensing* **2**:213-230.

Kriebel, K.T. 1978. Measured spectral bidirectional reflection properties of four vegetated surfaces. *Applied Optics* **17**:253-259.

Kusaka, T., Y. Kawata and S. Ueno. 1984. Multitemporal data analysis by extended radiometric correction. *Proceedings of the Eighteenth International Symposium on Remote Sensing of Environment.*

Kimes, D.S. and J.A. Kirchner. 1981. Modeling the effects of various radiant transfers in mountainous terrain on sensor response. *IEEE Transactions on Geoscience and Remote Sensing* **19**:100-108.

Little, J.J. 1982. Automatic registration of Landsat MSS images to digital elevation models. *IEEE Workshop on Computer Vision: Representation and Control.*

MacKenzie, M. 1988a. Remote sensing of the deciduous vegetation of Great Smoky Mountains National Park. Technical Papers, 1988 ACSM/ASPRS Annual Convention, *Image Processing/Remote sensing*, **4**:212-221.

MacKenzie, M. 1988b. Personal communication.

Peucker, T.K., M. Tichenor, and W.D. Rase. 1973. The computer Version of three relief representations. *Display and Analysis of Spatial Data*. pp.187-197. John Wiely & Sons.

Rehder, John B. 1987. Remote sensing and mapping of selected evergreen forest community types in the Great Smoky Mountains National Park. National Park Service. Great Smoky Mountains National Park, Gatlinburg, TN. 27pp.

Rosenfeld, A. and A.C. Kak. 1982. Digital Picture Processing. Volume II. Acadmic Press, Inc. pp. 349.

Schachter, B. 1980. Computer generation of shaded relief maps. *Map Data Processing*. pp.355-368. Academic Press, Inc.

Schowengerdt, R. A. 1983. Techniques for image processing and classification in remote sensing. Academic Press, Inc. 248 pp.

Seidel, K., Frank Ade, and J. Lichtenegger. 1983. Augmenting Landsat data with topographic information for enhanced registration and classification. *IEEE Transactions on Geoscience and Remote Sensing* **21**:252-258.

Smith, J.A., Tzeu Lie Lin, and K.J. Ranson. 1980. The Lambertian assumption and Landsat data. *Photogrammetric Engineering and Remote Sensing* **46**:1183-1189.

Strahler, A.H., J.E. Estes, P.F. Maynard, F.C. Mertz, and D.A. Stow. 1980. Incorporating collateral data in Landsat classification and modeling procedures. *Proceedings of the Fourteenth International Symposium on Remote Sensing of Environment.*

Strahler, A.H. 1981. Stratification of natural vegetation for forest and rangeland inventory using Landsat digital imagery and collateral data. *Int. J. Remote Sensing* **2**:15-41.

Teillet, P.M., B. Guindon and D.G. Goodenough. 1982. On the slope-aspect correction of multispectral scanner data. *Canadian Journal of Remote Sensing* **8**:84-106.

Teillet, P.M. 1986. Image correction for radiometric effects in remote sensing. *Int. J. Remote Sensing* **7**:1637-1651.

Tempfli, K. 1980. Spectral analysis of terrain relief for the accuracy estimation of digital terrain models. *ITC Journal* **3**:478-510.

U.S.G.S. 1987. Digital elevation models: data users guide. United States Department of the Interior, U. S. Geological Survey.

Woodham, R.J. and T.K. Lee. 1985. Photometric method for radiometric correction of multispectral scanner data. *Canadian Journal of Remote Sensing* **11**:132-161.

Woodham, R.J. and M.H. Gray. 1987. An analytic method for radiometric correction of satellite multispectral scanner data. *IEEE Transactions on Geoscience and Remote Sensing* **25**:258-271.

Yam, Simon and L.S. Davis. 1981. Image registration using generalized Hough transforms. 1981 *IEEE* - (?).

Yoeli, P., 1967. the mechanization of analytical hill shading. *The Cartographic Journal* 4:82-88.

Vita

Xiaomin Liu was born on July 24, 1957, in Beijing, China. He attended Primary School of Beijing Agricultural University and graduated from High School of Beijing Agricultural University, 1976. After settling and working in the suburbs of Beijing, he entered Tongji University at Shanghai in March, 1978 and received a Bachelor of Engineering degree in Engineering Survey in January, 1982. Offered a teaching position upon graduation, he worked in the Department of Civil Engineering, Nanjing Institute of Technology in Jiangsu Province, as assistant for two years.

He entered the graduate program in remote sensing of Beijing Forest College in 1984 and was accepted by the Graduate School of the University of Tennessee, Knoxville, in September of 1986. After graduating from University of Tennessee in the summer of 1988, he was accepted by the Department of Forest Resource and Management of University of California, Berkeley to pursue Ph.D degree in remote sensing and Geographic Information System.